

Fluctuation statistics in the scrape-off layer of Alcator C-Mod

R. Kube* and O. E. Garcia

UiT The Arctic University of Norway,

Department of Physics and Technology, N-9037 Tromsø

B. LaBombard and J. L. Terry

MIT Plasma Science and Fusion Center, Cambridge, MA, 02139, USA

(Dated: December 7, 2024)

Abstract

We study long time series of the ion saturation current and floating potential, obtained by Langmuir probes dwelled in the far-scrape off layer and installed in the divertor baffle of Alcator C-Mod, for a series of discharges with increasing line averaged plasma particle density. Using the ion saturation current as a proxy for the plasma particle density, we compare particle density amplitude histograms to best fits of a Gamma distribution, the Log-normal distribution and the sheath distribution [1]. Best fits of all three models agree with the observed histograms over multiple decades in normalized probability. Analysis of ion saturation current time series sampled at outboard midplane and at the divertor show that their dynamics are governed by intermittent large amplitude burst events and present a comparable conditionally averaged waveform. In both cases are histograms of the waiting times between successive large amplitude burst events and of the burst amplitudes well described by an exponential distribution. Best fit parameters for these models are of the same magnitude and are found to vary weakly with the plasma parameters. At the divertor, the conditionally averaged waveform of the electric potential that is associated with large burst events is dipolar for $\bar{n}_e/n_G \lesssim 0.35$. For $\bar{n}_e/n_G = 0.42$ the analysis suggests that blobs are no longer electrically connected to the divertor sheaths at a radial distance ca. 10mm outover the last closed flux surface.

I. INTRODUCTION

The scrape-off layer of magnetically confined plasmas is dominated by order unity fluctuations of the particle density and concomitant large, intermittent transport events. A large body of research links these phenomena to the radial propagation of plasma filaments which are elongated along the magnetic field and highly localized in the radial-poloidal plane, and hence called *blobs* [2–6]. Blobs are detrimental to the performance of magnetic confinement as they lead to increased heat fluxes to the divertor targets and increase main chamber recycling as they propagate through the scrape off layer and strike the vessel wall.

To assess the importance of plasma blobs on plasma confinement, questions regarding their mode of propagation have to be addressed. The underlying mechanism by which plasma blobs propagate radially out over is the interchange mechanism and a resulting electric drift [3]. Magnetic gradient and curvature drifts in an inhomogeneous magnetic field give rise to an electric current that polarizes structures of elevated pressure perpendicular to the magnetic field and its direction of variation [7 and 8]. This mechanism acts as to propagate the filament radially out over towards the main chamber wall at the outboard midplane location of a toroidally confined plasma.

The path by which the electric currents within the filamentary structure are closed are now crucial for the radial velocity of the filament. Assuming that the plasma filament extends uniformly along the magnetic field lines to the sheath, where the field lines intersect material targets, the electric current loop may be closed through these sheaths. In this case, an analytic solution of a two-field model predicts a dependence of the radial blob velocity, v_{rad} , on the blobs cross-field size ℓ , as $v_{\text{rad}} \sim \ell^{-2}$ [3]. When parallel currents within the plasma filament are negligible, the velocity scaling is given by the ideal interchange velocity scaling $v_{\text{rad}} \sim \sqrt{\ell}$ [9 and 10]. The parallel electric currents may also close at the X-point, where magnetic shear effects squeeze the plasma flux tubes as to shrink the diameter of the flux tube [10–14].

Recent work shows that the transition between ideal interchange to sheath-limited velocity scaling occurs with increasing ℓ . This effect was first observed at the simple toroidal experiment TORPEX [15] and has been verified by numerical simulation of seeded blobs [16]. Studies of plasma blobs in Alcator C-Mod find a good agreement between the radial velocity of the plasma blobs and the velocity scaling law valid for plasma blobs in the

sheath-connected regime [17]. More recent work at Alcator C-Mod reveals a strong correlation between time series of particle density proxies along the same magnetic field line at positions just above the outboard mid-plane and the outer divertor target [18].

The observed characteristic of the turbulence in the far scrape-off layer of magnetically confined plasmas are believed to be universal [19–21]. For one, the conditionally averaged waveform of large amplitude events in particle density time series presents a steep rise and a slow decay. [4–6, 22–26]. Correlation analysis further reveals the presence of a dipolar potential structure, centered around local maximum in the particle density. [27–29].

A consequence of frequent large amplitude events are particle density amplitudes histograms that present an long, elevated tail and the underlying time series feature positive coefficients of sample skewness and excess kurtosis [1, 19, 30, and 31]. The universal character of these features manifests itself in the fact that histograms of the particle density coincide upon normalization even when obtained at a single position in the far scrape-off layer for various plasma parameters [1, 19, 21, 26, and 31].

More recently, it was found that another salient feature of the sampled histograms is a quadratic relation between sample skewness, S , and excess kurtosis, F , of the form $F = a + bS^2$, where a and b are real coefficients. This relation is intrinsic to some probability distribution functions that have been proposed to describe the observed histograms of the particle density amplitudes. Data sampled in the TORPEX device over a broad range of discharge conditions and spatial locations was shown to be well described by the a generalized beta distribution [32]. The quadratic relation between skewness and excess kurtosis is further intrinsic to the gamma distribution which describes the fluctuations in the scrape-off layer of TCV [31]. Recent work models the observed particle density time series as a shot noise process, which is based on the superposition of individual burst events [33 and 34]. With further assumptions on the burst shape and burst arrival times this stochastic model predicts the Gamma function to be the stationary distribution function of the particle density amplitude and that the shape and scale parameter of the distribution can be expressed by the sample mean and root mean square [34]. It was shown that this model describes the particle density fluctuations in the outboard midplane scrape-off layer of Alcator C-Mod, as measured by gas-puff imaging, over several decades in normalized probability.

Although many candidates for the distribution function of observed particle density amplitude histograms have been proposed [1, 19, 21, 31, 32, and 34], no consensus on one particular analytic model exists so far in the fusion community.

In this paper, we present the analysis of long time series of the ion saturation current and floating potential obtained by Langmuir probes. Utilizing a probe dwelled in various positions in the scrape-off layer as well as probes at the divertor baffle allow us to study both effects discussed above: The question to what extend theoretically predicted effects of sheath connected blobs are visible as well as to compare sampled particle density amplitude histograms to theoretical models with high precision.

The structure of this article is as follows. Section II introduces models for fluctuation statistics in the far scrape-off layer and the employed conditional averaging method. The experimental setup is described in Section III. Section IV presents the time series analysis for the time series obtained in the outboard midplane scrape-off layer and Section V presents the time series analysis for the time series obtained from the divertor probes. A discussion of the results within a theoretical context and a conclusion is given in Section VI.

II. FLUCTUATION STATISTICS

Recent work models the observed particle density amplitude time series as a superposition of random burst events with a an exponentially decaying waveform [34]. Given that the occurrence of burst events is governed by a Poisson process, this model predicts a quadratic relation between coefficients of skewness and kurtosis. Further assuming an exponential burst shape, and exponentially distributed burst amplitudes, this model implies that the stationary particle density amplitude Φ is gamma distributed:

$$P_{\Gamma}(\Phi) = \frac{1}{\Phi\Gamma(\gamma)} \left(\frac{\gamma\Phi}{\langle\Phi\rangle} \right)^{\gamma} \exp\left(-\frac{\gamma\Phi}{\langle\Phi\rangle}\right), \quad (1)$$

where $\langle\Phi\rangle$ denotes an ensemble average and $\Gamma(x) = \int_0^{\infty} du u^{x-1} e^{-u}$ is the Gamma function. For this distribution, the scale and shape parameter are given by

$$\text{scale} = \frac{\Phi_{\text{rms}}^2}{\langle\Phi\rangle} \quad \gamma = \frac{\langle\Phi\rangle^2}{\Phi_{\text{rms}}^2}. \quad (2)$$

Here \cdot_{rms} denotes the root mean square. In terms of this shot noise model, the shape parameter is further given by the ratio of the burst e-folding time τ_d and the average waiting time between bursts, τ_w : $\gamma = \tau_d/\tau_w$. Large values of γ then describe a time series characterized by the frequent occurrence of bursts and large burst overlap while a small value of γ describe a time series where burst are intermittent events and overlap little.

The exponential waveform for the individual burst events is a common feature of turbulence in the far scrape-off layer [4–6, 22–26], and the burst amplitude and waiting time distributions have been observed in the scrape-off layer of Alcator C-Mod [35]. Optical measurements of the particle density amplitude in the scrape-off layer of Alcator C-Mod show good agreement with a Gamma distribution over almost four decades in normalized probability density [35]. Particle density fluctuations in the scrape-off layer of the *Tokamak à configuration variable* (TCV) were also found to be well described by Eqn. (1) over a large range of discharge parameters [31].

Sampled histograms of the particle density amplitude at the reversed field-pinch experiment RFX have been shown to be well described by two other probability distributions [1], the first being the log-normal distribution:

$$P_{\text{logn}}(\Phi) = \frac{1}{\Phi\sqrt{2\pi\sigma^2}} \exp\left(-\frac{(\log \Phi - \mu)^2}{2\sigma^2}\right), \quad (3)$$

where the shape parameter is given by $\sigma > 0$, and the scale parameter is given by μ . These are related to the sample mean via $\mu = \log\left(\bar{\Phi}^2/\sqrt{\Phi_{\text{rms}}^2 + \bar{\Phi}}\right)$ and $\sigma = \log\left(\Phi_{\text{rms}}^2/\bar{\Phi}^2 - 1\right)$. Here, and in the following $\bar{\cdot}$ denotes the sample mean. The second distribution follows from the observation that the sampled floating potential is commonly well described by a normal distribution. This is used in combination with the analytic solution of a two-field model for sheath connected blobs in [3], which relates the particle density amplitude to the electric potential. The probability distribution function for the particle density amplitude reads in this case [1]:

$$P_{\text{sh}}(\Phi) = \frac{H}{(\Phi/\Phi_0)(1 - \log(\Phi/\Phi_0)/K)} \exp\left(-\frac{\log(1 - \log(\Phi/\Phi_0)/K)^2}{2\sigma^2}\right). \quad (4)$$

Here H is a normalization constant, σ denotes the scale parameter, Φ_0 is a reference density scale, and K gives the ratio between sheath currents to the interchange term in the two-field

blob equations.

To determine the average structure of the bursts occurring in ion saturation current time series we employ conditional averaging [36]. Starting from the largest burst event in the time series at hand, we identify a set of disjunct sub records, placed symmetrically around the burst events that exceed a given threshold, until no more burst events exceeding this threshold are left uncovered. Taking the threshold to be 2.5 times the root mean square of the time series at hand, we write the conditionally averaged burst shape as

$$C(\tau) = \langle \Phi(\tau) | \Phi(\tau = 0) > 2.5 \times \Phi_{\text{rms}} \rangle. \quad (5)$$

The variability of the burst events is characterized by the conditional variance [37]:

$$\text{CV}(\tau) = \frac{\langle (\Phi - C)^2 | \Phi(\tau = 0) > 2.5 \times \Phi_{\text{rms}} \rangle}{C^2} \quad (6)$$

This quantity is bounded, $0 < \text{CV}(\tau) < 1$, where the values 0 and 1 indicate respectively perfect, and no reproducibility of the conditionally averaged waveform.

III. EXPERIMENTAL SETUP

Alcator C-Mod is a compact tokamak with a major radius of $R = 0.68$ m and a minor radius of $a = 0.22$ m, which allows for strong magnetic field, up to 8T on-axis.

The left panel of Fig. 1 shows a cross-section of Alcator C-Mod together with the diagnostics from which we report measurements: the horizontal scanning probe, the vertical scanning probe, and the Langmuir probe array on the lower outer divertor baffle. The right panel presents the Mach probe head installed on both scanning probes. As a common radial coordinate, we employ the magnetic flux label ρ , which gives the distance to the last-closed flux surface (LCFS) as mapped to the outboard midplane by the magnetic field. This coordinate is calculated by magnetic equilibrium reconstruction with the EFIT code [38] using input from a set of magnetic diagnostics installed in the vacuum vessel [39].

Both reciprocating probes have a Langmuir-Mach probe head installed [40 and 41], which is designed to routinely withstand heat fluxes of up to 100 MW/m^2 . This is required to withstand the heat fluxes in Alcator C-Mod plasmas, which are of the order of 1 GW/m^2 [41]. The horizontal scanning probe is installed ca. 10 cm above the outboard midplane and

can be reciprocated horizontally 11 cm into the plasma. For the presented experiments, the probe is dwelled at a single position in the scrape-off layer for the duration of the entire plasma discharge. For a position in the near scrape-off layer, the probe is targeted to dwell at $\rho \approx 3$ mm and at $\rho \approx 8$ mm for a position in the far scrape-off layer. The north-east and south-east probe heads are biased to -290 V with respect to the vacuum vessel, as to sample the ion saturation current. The south-west and north-west pins are electrically floating. This allows us to estimate the poloidal electric field as

$$E \approx \frac{V^{\text{NW}} - V^{\text{SW}}}{\Delta_{\text{d}}}, \quad (7)$$

where the poloidal separation between the electrodes is $\Delta_{\text{d}} = 2.24$ mm. During the campaign reported here, a large heat flux event shorted out both eastern electrodes. For the last two discharges reported in this article, the south-west electrode samples the ion saturation current and the north-west electrode samples the floating potential.

The vertical scanning probe is configured to plunge through the scrape-off layer up to the last closed flux surface, three times per plasma discharge. A triangular voltage waveform, scanning from 55 to -255 V with a frequency of 2 kHz is applied to all four pins of the probe head. We obtained the plasma electron density n_e , the electron temperature T_e and the floating potential by fitting a three parameter exponential function on the measured voltage-current characteristic of each probe head with a spatial resolution of $\Delta_{\rho} = 1$ mm.

The Langmuir probe array installed on the lower divertor baffle consists of two pins per probe which are configured to sample the ion saturation current and floating potential with a sampling frequency of 0.4 MHz respectively. The shallow angle between the poloidally projected magnetic field and the divertor baffle translates small disturbances of the magnetic field geometry into large motions of the strike point of the magnetic field on the divertor surfaces. In magnetic equilibrium, the two outermost divertor probe map to a distance of $\rho \approx 8 - 10$ mm. This corresponds to the approximate position within error margins of 5 mm where the horizontal scanning probe was dwelled.

We report from measurements obtained in 7 ohmically heated, lower single null discharges. For five of the discharges, the plasma current was set to $I_p = 0.6$ MA and the line-averages particle density was increased from $\bar{n}_e/n_G = 0.15$ to $\bar{n}_e/n_G = 0.42$. The other

two discharges feature a line-averaged particle density of $\bar{n}_e/n_G \approx 0.3$ with plasma currents of $I_p = 0.8$ MA and $I_p = 1.2$ MA respectively. The magnetic field strength is $B_0 = 5.4$ T on the magnetic axis for all discharges. The magnetic geometry is fixed for discharges with constant plasma current. For discharges with $I_p = 0.6$ MA the target safety factor containing 95% of the magnetic flux, q_{95} was aimed to be 6.0, for $I_p = 0.8$ MA $q_{95} = 4.5$ and $q_{95} = 3.5$ for $I_p = 1.2$ MA.

For all discharges, it was attempted to minimize fluctuations of the strike point, where the magnetic field intersects the lower divertor baffle. As a consequence of that, the estimated position of the last closed flux surface at outboard midplane is subject to larger fluctuations.

In the upper panel of Fig. 3 we present the time evolution of the line-averaged particle density. The middle panel shows the radial coordinate of the probe head of the horizontal scanning probe and the lower panel shows the radial coordinate of the two outermost divertor probes. The indicated time intervals in this figure correspond to the interval of the time series used for data analysis. These time intervals are chosen as to keep the line-averaged particle density of any given discharge within $\Delta\bar{n}_e/n_G \approx 0.02$ and the radial position of the horizontal scanning probe within an interval of $\Delta\rho \approx 5$ mm.

In Tab. I we list the plasma parameters of all shots as well as the probe position, the time interval on which the obtained time series are analyzed, and the plot marker used in subsequent figures. We also indicate the used electron temperature T_e at $\rho = 5$ mm which we use to normalize the electric potential and to estimate the acoustic velocity at the position of the horizontal scanning probe. Accompanying profiles of the electron temperature as measured by the vertical scanning probe are shown in Fig. 4.

IV. SCRAPE-OFF LAYER STATISTICS

We begin by analyzing the long time series obtained by the horizontal scanning probe to elucidate the statistical nature of the plasma fluctuations in the far scrape-off layer. For this, we take the plasma particle density to be proportional to the ion saturation current, and compare histograms of this current to the proposed distribution functions Eqs. (1), (3),

Shot	I_p/MA	q_{95}	\bar{n}_e/n_G	T_e/eV	ASP position	$t_{\text{start}}/\text{s}$	t_{end}/s	Plot marker
1111208007	0.55	6.2	0.15	35	near SOL	0.75(0.75)	1.10(1.10)	magenta dot
1111208008	0.55	6.4	0.28	25	far SOL	0.65(0.65)	1.50(1.50)	blue triangle down
1111208010	0.55	6.2	0.32	25	far SOL	0.80(-)	1.10(-)	green square
1111208011	0.55	6.2	0.31	20	far SOL	0.80(0.80)	1.10(1.10)	red circle
1111208012	0.55	5.9	0.42	20	far SOL	0.50(0.50)	0.70(0.70)	cyan triangle up
1111208025	0.80	4.6	0.33	20	far SOL	0.60(0.80)	0.95(1.30)	red triangle up
1111208034	1.10	3.5	0.26	20	far SOL	0.70(0.80)	1.10(1.20)	blue triangle up

TABLE I. List of the plasma parameters and the time interval used for time series analysis. The numbers in parenthesis give the interval on which data from the divertor probe is used. A dash indicates that no data is available.

and (4).

For the Gamma distribution, Eqn. (1), and the log-normal distribution, Eqn. (3), maximum likelihood estimators of the distribution parameters are readily available and are used in the following to give a best fit of the parameters of the respective distribution on to the histogram of the time series at hand. For the sheath distribution Eqn. (4), we employ a non-linear least squares method to find the parameters that give the best fit on the histogram of the sampled current at hand. Initial values for this fit are given by $S_0 = 1.0$, $\sigma_0 = I_{\text{rms}}$, $\Phi_0 = \bar{I}$, and $K_0 = 1.0$

In Fig. 5 we present the histogram of the ion saturation current as sampled by the north-east pin of the horizontal scanning probe for the discharge with $\bar{n}_e/n_G = 0.28$. The length of the time series is ca. 1 s and spans four decades in normalized probability. It presents elevated tails with fluctuations exceeding three times the mean of the time series. The histogram of data sampled by the south-east pin is qualitatively and quantitatively similar. For the stationary part of the time series we find $\bar{I} = 4.0 \times 10^{-2}$ A as measured by the north-east pin and $\bar{I} = 5.8 \times 10^{-2}$ A as measured by the south-east pin. With a sample variance for the north-east pin given by $I_{\text{rms}} = 1.3 \times 10^{-2}$ A, and $I_{\text{rms}} = 1.7 \times 10^{-2}$ A for the south-east pin, the respective normalized fluctuation levels are 0.32 for the and 0.30

respectively. Coefficients of skewness and excess kurtosis for the time series sampled by the north-east pin are given by $S = 0.78$ and $F = 0.96$, and $S = 0.71$ and $F = 0.80$ for the south east pin. This indicates that the particle density fluctuations are unlikely to be normally distributed.

For the time series sampled by the north-east pin (south-east pin), a maximum likelihood estimate of parameters for the Gamma distribution, Eqn. (1), yields a shape parameter $\gamma = 10.1(11.4)$, and a scale parameter of $4.02 \times 10^{-3} \text{ A}(5.11 \times 10^{-3} \text{ A})$. These values compare well to values found by estimating the parameters via Eqn. (2), $\gamma = \langle I \rangle^2 / I_{\text{rms}}^2 = 9.77(11.1)$, and a scale parameter of $\langle I \rangle / \gamma = 4.14 \times 10^{-3} \text{ A} (5.23 \times 10^{-3} \text{ A})$. This shows, that the stochastic model gives a correct description of the ion saturation current time series at hand. This value of γ corresponds to a time series characterized by the frequent occurrence of burst events. A maximum likelihood estimate of parameters for the log-normal distribution, Eqn. (3), yields $\sigma = 3.21 \times 10^{-1}(3.00 \times 10^{-1})$ and $\mu = 3.85 \times 10^{-2}(5.57 \times 10^{-2})$. A least-squares fit of Eqn. (4) yields $K \approx 5.31(4.68)$. This indicates that the observed blob dynamics are dominated by sheath effects.

Both, the Gamma distribution, and the sheath distribution, give a good description of the sampled histogram and its elevated tail over four decades in normalized probability. Eqn. (3) overestimates the elevated tail of the histogram in the range where $I/\bar{I} > 2.0$.

Increasing the line-averaged particle density to $\bar{n}_e/n_G = 0.42$, we find that the histogram presents strongly elevated tails, fluctuations exceed four times the mean of the time series, shown in Fig. 6. The ion saturation current time series sampled by the north-east pin has a mean of $\bar{I} = 9.44 \times 10^{-2} \text{ A}$ and a root mean square of $I_{\text{rms}} = 4.58 \times 10^{-2} \text{ A}$. This gives a normalized fluctuation level of $I_{\text{rms}}/\bar{I} \approx 0.485$. We find coefficients of skewness and kurtosis of the entire sample to be $S = 1.51$ and $F = 3.53$. The corresponding statistics of the time series sampled by the south-east pin are $\bar{I} = 1.41 \times 10^{-1} \text{ A}$, $I_{\text{rms}}^2 = 5.03 \times 10^{-2} \text{ A}$, and $I_{\text{rms}}/\bar{I} = 0.357$. Coefficients of sample skewness and excess kurtosis are $S = 1.37$ and $F = 2.70$. Here, the fluctuations on the north-east pin are significantly larger than the fluctuations sampled by the south-east pin.

For the north-east pin (south-east pin), the shape and scale parameter for the best fit of a Gamma distribution as given by a maximum likelihood estimate are $1.94 \times$

$10^{-2} \text{ A}(1.55 \times 10^{-3} \text{ A})$ and $\gamma = 4.86(9.10)$. Invoking Eqn. (2), we find a scale parameter of $2.22 \times 10^{-2} \text{ A}(1.80 \times 10^{-2} \text{ A})$ and $\gamma = 4.25(7.85)$. A maximum likelihood estimate of Eqn. (3) yields $\sigma = 4.66 \times 10^{-1}(3.28 \times 10^{-1})$ and $\mu = 8.49 \times 10^{-2}(1.33 \times 10^{-1})$. Fitting Eqn. (4) on the histogram we find $K \approx 1.2 \times 10^4(1.3 \times 10^4)$. We find that best fit of Eqn. (3) describes the positive tail of both histograms well, while Eqn. (4) and Eqn. (1) underestimate the elevated tail of both histograms.

To study the nature of intermittency in the ion saturation current time series we proceed to study normalized time series. For this, we rescale the ion saturation current time series as

$$\tilde{I} = \frac{I - \bar{I}_{\text{mv}}}{I_{\text{rms,mv}}}. \quad (8)$$

The subscript mv denotes the moving average and moving root mean square respectively. The moving mean and moving root mean square are computed within a window of 16384 elements when applied to data from the horizontal scanning probe. This window corresponds to roughly 3ms and exceeds typical autocorrelation times of ca. $15 \mu\text{s}$ by a factor of 2000 [42]. The same window length is used for the time series obtained by the divertor probes. In the latter case, this corresponds to approximately 20 ms. Time series of the floating potential are rescaled by first removing a linear trend from the time series and subsequently normalizing the time series to the electron temperature and as to have vanishing mean:

$$\tilde{V} = \frac{e(V - \bar{V})}{T_e}. \quad (9)$$

In Fig. 7 we present conditionally averaged waveforms and their conditional variance, of the normalized time series for the discharge with $\bar{n}_e/n_G = 0.28$. The upper row shows the conditionally averaged waveform of large amplitude bursts occurring in the ion saturation current, as measured by the north-east and south-east pins, as well as their conditional variance. The averaged waveform is asymmetric with an e-folding rise time of $\tau_r \approx 2 \mu\text{s}$ and decay time of $\tau_d \approx 4 \mu\text{s}$. Their reproducibility is close to 1 within the interval centered around $\tau = 0 \mu\text{s}$, bounded by the e-folding times, and shows the same asymmetry as the burst shape.

The conditionally averaged floating potential waveform, computed by setting the trigger condition on bursts in the ion saturation current time series as sampled by the north-east

pin, is shown in the middle row of Fig. 7. We find that the south-west electrode measures a dipolar waveform, where the positive peak traverses the probe pin before the negative peak. The peak-to-valley range of the waveform is approximately 0.3 where the positive peak is larger in absolute value than the negative peak by a factor of 2. The waveform as measured by the north-west pin is more symmetric, and features a peak-to-valley range of approximately 0.2. The positive peak is also more reproducible with $1 - CV \approx 0.3$, compared to $1 - CV \approx 0.2$ for the waveform measured by the north-west pin.

Triggering on the south-east pin, the conditionally averaged floating potential waveforms are also dipolar with peak-to-valley ranges of ca. 0.2 for the south-west pin, and ca. 0.4 for the north-west pin. The reproducibility of the waveform is larger by a factor of two for the latter. Opposite to the situation where the trigger is on the north-east pin, here the reproducibility is larger on the north-west pin where the negative part of the blobs potential dipole is measured after its density maximum has traversed the probe.

This is compatible with the picture of a dipolar potential structure, centered around the particle density maximum of the plasma blob that traverses into the direction of $\mathbf{B} \times \nabla B$, i.e. poloidally downwards. For the plasma blob to propagate radially outwards, the negative pole of the potential has to be poloidally above the particle density maximum and the positive pole has to be poloidally below the particle density maximum. When the particle density maximum is recorded by the north-east pin, the positive pole of the potential structure has traversed the south-west pin. This explains the pronounced positive pole for $\tau \lesssim 0$ of the south-west pin and its relatively large reproducibility. The negative pole of the potential structure traverses the north-west pin for $\tau \gtrsim 0$ and leads to a relatively large reproducibility of the waveform.

The conditionally averaged waveform of the estimated electric field, shown in Fig. 8, is a monopolar structure with a peak value of approximately -2500 Vm^{-1} when triggered on bursts occurring on the north-east pin, and approximately -3000 Vm^{-1} when triggered on bursts occurring on the south-east pin. Using that the toroidal magnetic field at the probe position is approximately 4.0 T, this corresponds to a local electric drift velocity of $v_{\text{rad}} \approx 600 - 700 \text{ ms}^{-1}$.

We continue by elucidating the relation between the burst amplitudes and their associated radial velocity. For this, we assume that the time it takes for a filament to traverse the probe is well approximated by $\tau_r + \tau_d$. Both e-folding times are found by a least squares fit of an exponential waveform on the rise and decay of the average burst shape respectively. The electric drift velocity associated with a burst event is then computed with the estimated electric field averaged over the interval denoted by the gray rectangle in Fig. 8.

Fig. 9 shows the normalized electric drift velocity v_{rad}/C_s associated with each burst event plotted against its normalized burst amplitude. We find that the filaments radial velocities do not exceed 5% of the sound speed. Amplitudes and velocities appear to be uncorrelated in the near scrape-off layer, as shown in the upper left panel. The Pearson sample correlation coefficient is in this case $r = 0.09$. We find that approximately an equal number of estimated velocities are radially inwards and radially outover. The other three panels show data sampled from discharges where the probe is dwelled in the far scrape-off layer. Here we observe that ca 90% of all events have a velocity directed radially outover and that the sample correlation coefficient increases with the line averaged plasma density. We attempt a linear fit on the observed velocities by binning the sampled velocities in amplitude bins with a width of $0.25\tilde{I}$ using an uncertainty in for point that is given by the root mean square value of all samples in the corresponding bin. We find that the velocity increases with the normalized burst amplitude as $v_{\text{rad}}/C_s \approx 0.02 \times \tilde{I}$. Fluid modeling of plasma blobs predicts a scaling of $v_{\text{rad}}/C_s \approx \sqrt{\tilde{I}}$ [9]. Due to the large scatter in the estimated velocities, due to the background turbulence, and given that the range of observed amplitudes is smaller than one decade we however attempted a linear fit. Indeed, the residuals for this fit are normally distributed however due to the large scatter we find reduced χ^2 values of the order 10^{-3} for all fits.

Conditional averaging further reveals the distribution of waiting times between successive burst events and the distribution of burst amplitudes of the rescaled time series at hand. For discharges where multiple electrodes sample the ion saturation, we only use data sampled by the north east pin. Fig. 10 shows the histograms of the sampled waiting times between successive burst events with amplitudes exceeding 2.5 times the root mean square of the time series at hand.

The shape of the sampled histograms indicates that the waiting times are well described by an exponential distribution. For an exponentially distributed random variable $X > 0$, the complementary cumulative distribution function $1 - F_X(X)$ is given by

$$1 - F_X(X) = \exp\left(-\frac{X - X_0}{\langle X \rangle}\right). \quad (10)$$

Here $\langle X \rangle$ is the scale length of the distribution, and is X_0 the location parameter of the distribution. To obtain the scale length of the distribution from sampled data, we employ a maximum likelihood estimate. This method is unbiased, in the sense that all data points are equally weighted when estimating the scale parameter [43]. The location parameter is given by the conditional averaging sub record length in the case of waiting time distributions and the conditional averaging threshold in the case of burst amplitude distributions.

In the upper panel of Fig. 10 we compare histograms of the sampled waiting times for discharges with $I_p = 0.55$ MA to best fits of Eqn. (10). A full lines denotes the best fit of Eqn. (10) on the like colored histogram. In the lower panel we compare waiting time histograms sampled in discharges with $\bar{n}_e/n_G = 0.28$ and $I_p = 0.6$ MA, $\bar{n}_e/n_G = 0.26$ and $I_p = 0.8$ MA, as well as discharges with $\bar{n}_e/n_G = 0.30$ and $I_p = 0.6$ MA $\bar{n}_e/n_G = 0.33$ and $I_p = 1.1$ MA. Best fits on the histograms sampled in discharges with $I_p = 0.8$, and 1.1 MA, are denoted by a dashed line.

For discharges with $I_p = 0.55$ MA we find that the scale length of the distribution increases from $\langle \tau_w \rangle \approx 120 \mu s$ for $\bar{n}_e/n_G = 0.28$ to $\langle \tau_w \rangle \approx 260 \mu s$ and ca. $200 \mu s$ for the discharges with $\bar{n}_e/n_G = 0.32$ and $\bar{n}_e/n_G = 0.31$. For $\bar{n}_e/n_G = 0.42$ we find $\langle \tau_w \rangle \approx 180 \mu s$. For discharges with $\bar{n}_e/n_G = 0.26$ and $I_p = 0.55$ MA, and $\bar{n}_e/n_G = 0.28$ and $I_p = 0.80$ MA, we find that the scale length increases to $\langle \tau_w \rangle \approx 180 \mu s$ when increasing the plasma current to $I_p = 0.80$ MA. For a plasma current of $I_p = 1.2$ MA we find that $\langle \tau_w \rangle \approx 190 \mu s$, which is similar to the scale length for a plasma current of $I_p = 0.55$ MA.

Fig. 11 compares histograms of the sampled normalized burst amplitudes to the best fit of best fits of Eqn. (10). We find that the burst amplitudes histograms are well described by an exponential distribution over approximately one decade and that the burst amplitudes vary little with the plasma parameters. For discharges with $I_p = 0.6$ MA we find that the

scale length increases from $\langle A \rangle = 1.1$ for $\bar{n}_e/n_G = 0.28$ to $\langle A \rangle = 1.3$ for $\bar{n}_e/n_G = 0.42$.

Comparing the histogram for discharges with similar line averaged density and different plasma current, we find scale lengths of 1.1, and 1.2 for the discharges with $\bar{n}_e/n_G = 0.31$ and $I_p = 0.55$ MA, and $\bar{n}_e/n_G = 0.33$ and $I_p = 0.80$ MA respectively. Comparing discharges with $\bar{n}_e/n_G = 0.28$ and $I_p = 0.55$ MA, and $\bar{n}_e/n_G = 0.26$ and $I_p = 1.1$ MA we find that the estimated amplitude scale length increases from 1.1 to 1.5.

V. DIVERTOR PLASMA FLUCTUATIONS

We proceed by analyzing time series obtained by the Langmuir probes on the lower divertor in the same manner as in the previous section.

Fig. 12 presents the histogram of the ion saturation current time series for the discharge with $\bar{n}_e/n_G = 0.15$, as sampled by the two outermost divertor probes 9 (shown in the upper panel) and 10 (shown in the lower panel). The range on the x-axis of the plot is the same as for Figs. 5, and 6, and the y-axis spans one decade less due to the lower sampling frequency of the divertor probes. The average current at probe 9 is $\bar{I} = 4.40 \times 10^{-2}$ A and the root mean square is $I_{\text{rms}} = 1.47 \times 10^{-2}$ A, which yields a relative fluctuation level of $I_{\text{rms}}/\bar{I} = 0.334$. As shown in the upper panel of Fig. 12, the sample presents only slightly elevated tails, fluctuations in the time series do not exceed 2.5 times the mean. Coefficients of skewness and excess kurtosis are given by $S = 0.41$ and $F = -0.28$. A best fit of Eqn. (1) yields a scale parameter of 5.10×10^{-3} A and $\gamma = 8.64$, while invoking Eqn. (2) yields a scale parameter of 4.92×10^{-3} A and $\gamma = 8.94$. A best fit of Eqn. (3) yields $\sigma = 3.52 \times 10^{-1}$ and $\mu = 4.15 \times 10^{-2}$, and the best fit of Eqn. (4) gives $K = 3.20$. All four analytic descriptions overestimate the elevated tail of the histogram.

The histogram of the ion saturation current as sampled by divertor probe 10 presents more elevated tails with fluctuations exceeding 2.5 times the mean of the time series. With $\bar{I} = 2.86 \times 10^{-2}$ A and $I_{\text{rms}} = 9.01 \times 10^{-3}$ A the relative fluctuation level is $I_{\text{rms}}/\bar{I} = 3.14 \times 10^{-1}$. Maximum likelihood estimates of the scale and shape parameter for the Gamma distribution give 2.75×10^{-2} A and $\gamma = 10.4$, while Eqn. (2) yields a scale parameter of 2.83×10^{-2} A and

$\gamma = 10.1$. Both resulting distributions give a good description of the observed histogram and describe the elevated tail of the histogram well. Best fits of the Eqn. (3) and Eqn. (4) yield $\sigma = 3.14 \times 10^{-1}$, $\mu = 2.77 \times 10^{-2}$, as well as $K = 1.27 \times 10^3$ respectively. The resulting distributions both over estimate the sampled histograms for events exceeding two times the sample mean.

Fig. 13 presents the histograms of the ion saturation current as sampled by both divertor probes for the discharge with $\bar{n}_e/n_G = 0.42$. Both time series present fluctuations of up to three times the mean value of the time series. For the time series obtained by probe 9 we find a sample mean of $\bar{I} = 2.02 \times 10^{-1} \text{A}$ and a root mean square value of $I_{\text{rms}} = 7.75 \times 10^{-2}$. This gives a normalized fluctuation level of $I_{\text{rms}}/\bar{I} = 0.38$. Coefficients of skewness and excess kurtosis are $S = 1.31$ and $F = 2.32$. This shows the non-gaussian character of the histogram. The best fit of Eqn. (1) on the time series yields a scale parameter of $2.59 \times 10^{-2} \text{A}$ and $\gamma = 7.84$ and underestimates the positive tail of the distribution. Eqn. (2) yields a scale parameter of $2.96 \times 10^{-1} \text{A}$ and $\gamma = 6.86$. The corresponding gamma distribution approximates the positive tail of the histogram better than the best fit, but also overestimates the lower tail of the histogram. Best fits of Eqn. (3) and Eqn. (4) describe the observed histogram better for values of $I/\bar{I} \leq 1.5$ but also fail to account for the elevated tails.

Continuing with the time series sampled by probe 10, shown in the lower panel, we find tail is less elevated than in the histogram sampled by probe 9, with normalized amplitudes not exceeding three times the sample mean. Values of the sample mean, root-mean square and relative fluctuation level are $\bar{I} = 2.04 \times 10^{-1} \text{A}$, $I_{\text{rms}} = 5.69 \times 10^{-2}$, and $I_{\text{rms}}/\bar{I} = 2.78 \times 10^{-1}$. Coefficients of sample skewness and excess kurtosis are $S = 1.02$ and $F = 1.82$. These five statistics are lower than those observed 2 mm radially inwards by divertor probe 9 and show that the observed time series is not normally distributed. The best fit of parameters for Eqn. (1) on the time series, yields a scale parameter of 1.47×10^{-2} and $\gamma = 14.0$, while Eqn. (2) gives a scale parameter of 1.58×10^{-2} and $\gamma = 12.9$. The best fit of Eqn. (3) gives a shape parameter of $\sigma = 2.68 \times 10^{-1}$ and a log scale parameter of $\mu = 1.97 \times 10^{-1}$, while we find $K = 3.89 \times 10^3$ via a best fit on Eqn. (4). We find that all resulting distributions resemble the observed histogram well but underestimate the elevated tail slightly.

We continue the analysis with the normalized time series given by Eqs. (8) and (9). The conditionally averaged waveforms of the normalized ion saturation current and floating potential, as well as their conditional variances for discharges with $\bar{n}_e/n_G = 0.15, 0.28,$ and 0.42 and sampled by probe 10 are shown in Fig. 14. For the discharge with $\bar{n}_e/n_G = 0.15,$ the conditionally averaged burst shape is asymmetric. Least squares fit of a decaying exponential function on the burst shape yield e-folding time of $\tau_r \approx 12 \mu s$ and $\tau_d \approx 14.0 \mu s.$ For the discharge with $\bar{n}_e/n_G = 0.28$ we obtain $\tau_r \approx 14 \mu s$ and $\tau_d \approx 12 \mu s.$ The conditionally averaged burst shape for the discharge with $\bar{n}_e/n_G = 0.42$ is asymmetric, we find a rise time of $\tau_r \approx 26 \mu s$ and a decay time of $\tau_d \approx 66 \mu s.$ All conditionally averaged burst shapes are reproducible with $1 - CV \approx 1.$

The conditionally averaged waveform of the floating potential is shown in the lower panel of Fig. 14. We assume the divertor to be detached in the discharge with $\bar{n}_e/n_G = 0.42$ and use a value of $T_e = 10 \text{ eV}$ to normalize the time series [44]. For the discharges with $\bar{n}_e/n_G = 0.15$ and $\bar{n}_e/n_G = 0.28$ we observe that a dipolar potential structure is associated with the occurrence of large amplitude bursts. These waveforms are reproducible with $1 - CV \approx 0.8.$ For the discharge with $\bar{n}_e/n_G = 0.42$ we observe a dipole that is smaller by a factor of approximately 6 than for the other two discharges. With a reproducibility of $1 - CV \approx 0.1,$ this registered floating potential waveform is also very irregular.

We continue by studying the intermittency of large amplitude burst events, as observed by divertor probe 10.

In Fig. 15 we present sampled histograms of the waiting times between successive large amplitude burst events in the ion saturation current time series as sampled by divertor probe 10. Full lines denote Eqn. (10) with a scale parameter obtained by a maximum likelihood estimate on the time series and a location parameter of $\tau_{w,0} = 100 \mu s.$ The upper panel shows again data from discharges with $I_p = 0.55 \text{ MA}$ and the lower panel presents histograms from discharges with $\bar{n}_e/n_G = 0.31$ and $I_p = 0.55 \text{ MA}$ as well as $\bar{n}_e/n_G = 0.33$ and $I_p = 0.8 \text{ MA}.$ A dashed line indicates the best fit in the lower panel. Axis limits in both panels are chosen as to match the respective figures that present data for the horizontal scanning probe, Fig. 10.

We find that for all plasma parameters, the observed waiting times are well described by an exponential distribution. For $I_p = 0.55$ MA, estimates of the scale length increase from $\langle\tau_w\rangle \approx 270 \mu\text{s}$ for the discharge with $\bar{n}_e/n_G = 0.15$ to $\langle\tau_w\rangle \approx 430 \mu\text{s}$ for $\bar{n}_e/n_G = 0.31$. For $\bar{n}_e/n_G = 0.42$ we find $\langle\tau_w\rangle \approx 380 \mu\text{s}$. Comparing discharges with $\bar{n}_e/n_G \approx 0.30$, we find that for $I_p = 0.8$ MA the maximum likelihood estimate of the scale length is $\langle\tau_w\rangle \approx 360 \mu\text{s}$, lower by ca. $70 \mu\text{s}$ than in the case for $I_p = 0.55$ MA.

Fig. 16 shows the distribution of the burst amplitudes in the normalized time series of the ion saturation current as sampled by divertor probe 10. The figure layout is identical to Fig. 15. Maximum likelihood estimates of the scale length are $\langle A \rangle \approx 0.6$ for $\bar{n}_e/n_G = 0.15$, $\langle A \rangle \approx 0.6$ for $\bar{n}_e/n_G \approx 0.30$ and increase to $\langle A \rangle \approx 0.9$ for $\bar{n}_e/n_G = 0.42$. For discharges of $\bar{n}_e/n_G \approx 0.30$ we find that the scale length increases from $\langle A \rangle \approx 0.6$ for $I_p = 0.6$ MA to $\langle A \rangle \approx 0.8$ for $I_p = 0.8$ MA. These values are comparable in magnitude to the scale lengths presented in Fig. 11.

VI. DISCUSSION AND CONCLUSIONS

A statistical analysis of long ion saturation current time series, sampled in the outboard midplane far scrape-off layer and at the outer divertor for line averaged plasma densities varying from $\bar{n}_e/n_G = 0.15$ to $\bar{n}_e/n_G = 0.42$, shows that the time series are characterized by large fluctuations and that their dynamics are dominated by the intermittent arrival of large amplitude burst events for all line averaged densities. Histograms of time series sampled in the outboard mid plane far scrape-off layer present elevated tails with fluctuations up to five times the mean of the time series. For $\bar{n}_e/n_G = 0.28$ the probe pins connected to the outboard midplane and to the divertor by the magnetic field sample time series with comparable statistics. For $\bar{n}_e/n_G = 0.42$ we find that the pin connected to the outboard midplane samples a time series that presents a larger relative fluctuation level and larger coefficients of sample skewness and excess kurtosis than the pin connected to the divertor. The time series obtained by the divertor probes show qualitatively the same features, albeit with a lower normalized fluctuation magnitude. For the divertor time series we additionally observe that the magnitude of the fluctuations is smaller(larger) at a for $\rho \approx 8\text{mm}$ than at $\rho \approx 10\text{mm}$ for a discharge with $\bar{n}_e/n_G = 0.15$ ($\bar{n}_e/n_G = 0.42$). Shown in Fig. 17, time

series sampled at both positions are interspersed by large amplitude burst events. The burst structure observed at the divertor appears to be more smoothed out and to vary on a larger time scale. This is partially due to the lower sampling frequency of the time series sampled by the divertor probe.

A comparison to different analytic models for the amplitude probability distribution function gives no conclusive result. We find that maximum likelihood estimates of parameters for Eqs. (1), and (3), as well as a least squares fit of Eqn. (4), yield probability distribution functions that are roughly compatible with the amplitude histogram over up to four decades in normalized probability density. Maximum likelihood estimates of the parameters for a Gamma distribution are similar to estimates using Eqn. (2). This indicates that the stochastic model described in [34] describes the underlying stochastic processes in the plasma turbulence to a large degree.

Fig. 18 shows the sample excess kurtosis plotted against the sample skewness, computed for time series of length 20ms, taken from all discharges where the horizontal scanning probe is dwelled in the far scrape-off layer. For discharges with $I_p = 0.55$ MA we find both S , and F to increase with \bar{n}_e/n_G . While the discharges with $\bar{n}_e/n_G = 0.31$ and $I_p = 0.55$ MA, and $\bar{n}_e/n_G = 0.33$ and $I_p = 0.8$ MA show similar values of skewness and excess kurtosis, the time series obtained in the discharge with $\bar{n}_e/n_G = 0.26$ and $I_p = 1.1$ MA present coefficients of skewness larger by a factor of three than found in the discharge with $\bar{n}_e/n_G = 0.28$ and $I_p = 0.55$ MA. A least squares fit of the model $F = a + bS^2$ on all value pairs yields coefficients of $a = -0.20 \pm 0.04$ and $b = 1.51 \pm 0.03$.

The relation between sample coefficients of skewness and excess kurtosis, obtained by the time series recorded by the divertor probes, is qualitatively similar to those from the horizontal scanning probe Fig. 19. We find that the sample coefficients have a smaller range and notably negative values of excess kurtosis. The clustering of the sample pairs is similar to the clustering for the horizontal scanning probe data, with smaller value pairs for the discharge with $I_p = 0.55$ MA and $\bar{n}_e/n_G = 0.28$, than for the discharge with $I_p = 1.1$ MA and $\bar{n}_e/n_G = 0.28$. A least squares fit of the quadratic model yields on all value pairs yields $a = -0.51 \pm 0.02$ and $b = 1.78 \pm 0.03$.

The observed values of sample skewness and excess kurtosis all fall in a range between $0.0 \leq S \leq 2.0$ and $0.0 \leq F \leq 6.0$. These ranges are considerably lower than observed for a similar analysis of gas-puff imaging data in Alcator C-Mod [35]. In the latter case, the view of the diagnostics includes the area of the wall shadow, characterized by a considerably low plasma background density. As plasma blobs propagate into this region, they are registered in the intensity time series as amplitudes which are significantly larger than the background intensity signal. This leads to large values of sample skewness and excess kurtosis. In the present case, only data from the far scrape-off layer is sampled where all amplitude events are less than ca. 4 times the mean of the time series. We further observe a larger scatter of the data points than in the case of gas-puff imaging data, which is caused by the probe to be more sensitive to fluctuations of the plasma parameters on short temporal scales.

The distribution of waiting times between large amplitude in all sampled ion saturation current time series is found to be well described by an exponentially distribution over several decades. This suggests that the individual large amplitude events are uncorrelated and that their occurrence is governed by a Poisson process. This is of special importance when considering a time series $\Phi(t)$, formed by the superposition of individual burst events as

$$\Phi(t) = \sum_k A_k \Psi(t - t_k). \quad (11)$$

Here we denote the burst amplitudes with A_k and the burst arrival times with t_k . When assuming that the burst arrival times t_k are uniformly distributed, one can show that skewness and excess kurtosis of the process Eqn. (11) follow a quadratic relation[34]. Finding exponentially distributed waiting times and a quadratic relation between skewness and excess kurtosis stresses the notion to interpret the sampled ion saturation current time series as the realization of a shotnoise process Eqn. (11).

The histograms of the normalized burst amplitudes, Fig. 11 and Fig. 16 suggest furthermore that also the burst amplitudes follow an exponential distribution. The evidence for this is however less clear than for the waiting times. The estimated shape parameter for all distributions is $\gamma \approx 10$. This describes the case of small intermittency, i.e. bursts arrive frequently and have large overlap. As a consequence of the large overlap the amplitudes

as taken from the time series overestimate the individual amplitudes of the underlying bursts. This is reflected in the curved shape of the histograms Figs. 10 and (15). We note however, that the presented maximum likelihood estimates agree well with the complementary cumulative distribution function over ca. one decade, i.e. describe 90% of all events well.

Conditional averaging of the ion saturation current time series further reveals an average burst shape that features a steep rise and a slow decay, both of which are well described by an exponential waveform. Typical rise times and decay times, as measured at the outboard midplane, are $\tau_r \approx 5\mu\text{s}$ and $\tau_d \approx 10\mu\text{s}$, and vary by a factor of approximately 2 with the plasma line averaged density, Fig. 20. Rise and decay times as sampled by the divertor probes are large by a factor of ca. 2 than the respective values sampled at outboard midplane and the outermost divertor probe shows a larger asymmetry of the conditionally averaged waveform. However, this waveform does not allow to draw conclusions about the filament dimensions at the divertor. The recorded waveform may either be due to a filament impinging normal to the probe or due to a filament propagating radially outover.

The conditionally averaged waveforms of the normalized ion saturation current and electric potential, sampled at the outboard midplane, support the conventional picture of plasma blob propagation through the scrape-off layer. That is, peaks in the plasma particle density are associated with an electrostatic dipolar structure whose polarization is compatible with a resulting electric drift velocity pointing outwards towards the vessel wall. The phase shift between the conditionally averaged waveforms of the ion saturation current and electric potential is approximately $\pi/2$ and the estimated radial velocities of the plasma blobs are in the order of a few per cent of the ion acoustic velocity for all line averaged plasma particle densities. These results extend previous measurements made in the scrape off layer of Alcator C-Mod [27]. We further find a correlation between the estimated radial filament velocity and their normalized amplitude and that sample correlation coefficient increases with \bar{n}_e/n_G . Furthermore is the majority of all velocities observed in the far scrape-off layer, ca. 90%, radially out over. A possible explanation for this correlation is that the pressure gradient within the filament structure increases with filament amplitude. Fluid modeling of isolated plasma filaments shows that the magnitude of the plasma pressure gradient increases the plasma vorticity associated with the plasma blob [9]. Assuming that the poloidal size of

the plasma blobs is constant, this creates a larger electric field which in turn increases the electric drift magnitude. Numerical simulations of isolated plasma blobs have shown that the radial blob velocity indeed increases as the square root of its normalized particle density amplitude [16].

To interpret the conditionally averaged waveform of the electric potential at the divertor plates we note, that potential variations may also be caused by the internal temperature profile of plasma blobs [45]. For an electron temperature of 50eV we evaluate the electron thermal velocity to be $v_{\text{th,e}} \approx 3 \times 10^6 \text{ms}^{-1}$ and $C_s \approx 10^4 \text{ms}^{-1}$. A lower bound on the characteristic velocity associated with transport of potential perturbations along the magnetic field is further given by $v_{\text{th,e}}$ [18]. Given a connection length of $L_{\parallel} = 10\text{m}$ from outboard midplane to the sheaths, the time scales for particle and energy transport along the magnetic field are respectively given by $\tau_{n,\parallel} \approx 2 \times 10^{-4}\text{s}$ and $\tau_{E,\parallel} \approx 3 \times 10^{-6}\text{s}$. We assume that a blob is created at outboard midplane as a structure modulated along the magnetic field that propagates radially out over with a constant velocity of $v_{\text{rad}} = 500\text{ms}^{-1}$ within the entire flux tube. This implies that energy and particles transported along the field from the moment of the blobs instantiation will have reached the divertor at radial coordinates of $\rho_E \approx 1.7 \times 10^{-3}\text{m}$ and $\rho_n \approx 1.0 \times 10^{-1}\text{m}$. We observe particle density fluctuations that are characteristic of blobs consistently at the divertor probe at $\rho \approx 8\text{mm}$. These estimates imply that the observed filaments have a velocity normal to the flux surfaces which is less than observed at the outboard midplane. Furthermore we observe that with increasing plasma collisionality the electric potential signature of blobs vanishes at the outermost divertor probe. For discharges with $\bar{n}_e/n_G \leq 0.33$, the conditionally averaged potential structure, as sampled by the divertor probes, are dipolar and present a pronounced positive peak value. Now, the electric current to the divertor sheaths is given by

$$J_{\text{sh}} = en_e C_s \left(1 - \exp\left(\frac{-eV}{T_e}\right) \right). \quad (12)$$

When neglecting electron temperature fluctuations, a dipolar potential structure implies that the parallel electric current within the elementary structure is closed at the divertor. When this is the case, the radial velocity scaling of the plasma filaments falls in the sheath connected regime, i.e. $v_{\text{rad}} \sim \ell^{-2}$. For the discharge with $\bar{n}_e/n_G = 0.42$, the conditionally averaged electric potential has no pronounced shape and features low reproducibility. This

implies that both mechanisms for potential transport along the magnetic field are ineffective for blobs that have traversed this distance through the scrape-off layer. Again neglecting temperature fluctuations, this further implies that the electric current loop within the plasma filament closes upstream of the divertor. This idea is supported by measurements of radial blob velocities in high density plasmas in Alcator C-Mod which indicate that the radial filament velocity at outboard midplane increases with increasing line-averaged density [46] and exceed the value predicted for sheath connected blobs [47].

ACKNOWLEDGMENTS

Work at MIT supported by USDoE Cooperative Agreement DE-FC02-99ER54512 and DE-AC02-09CH11466.

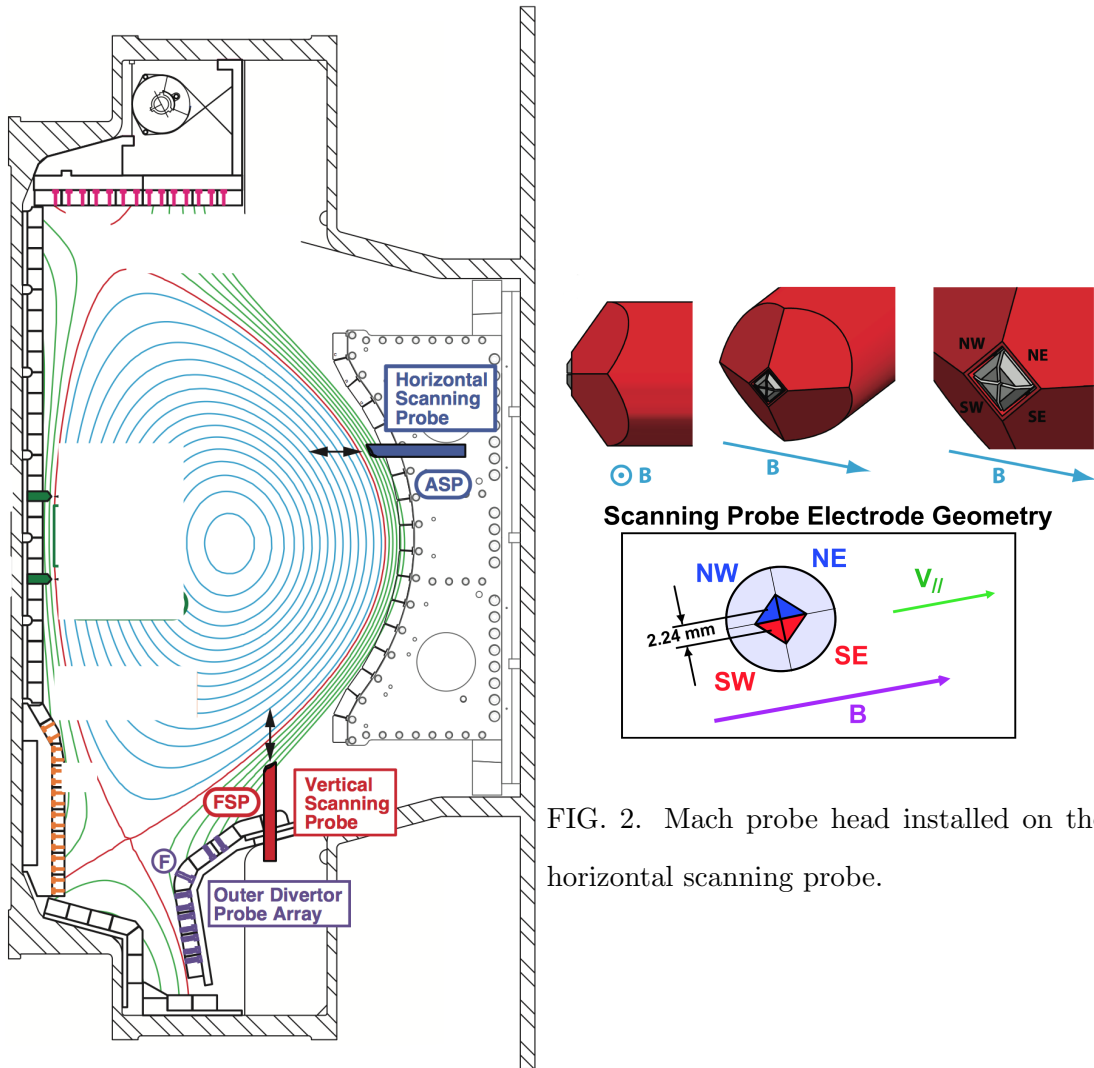


FIG. 1. Cross-section of Alcator C-Mod.

FIG. 2. Mach probe head installed on the horizontal scanning probe.

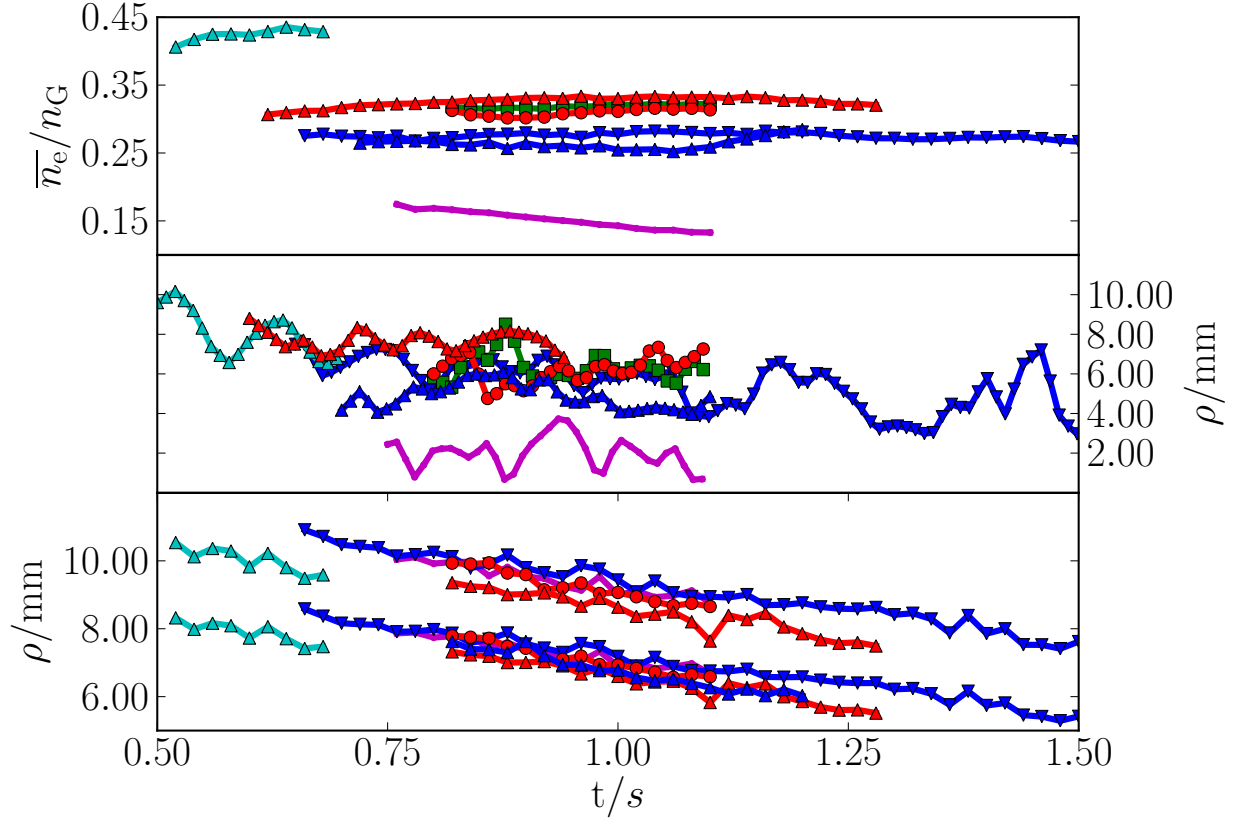


FIG. 3. Evolution of the line-averaged particle density (upper panel) and radial coordinate for the horizontal scanning (mid panel). We have added an offset of $\rho_0 = 5$ mm to the position of the horizontal scanning probe. The lower panel shows the radial coordinate for the two outer most divertor probes.

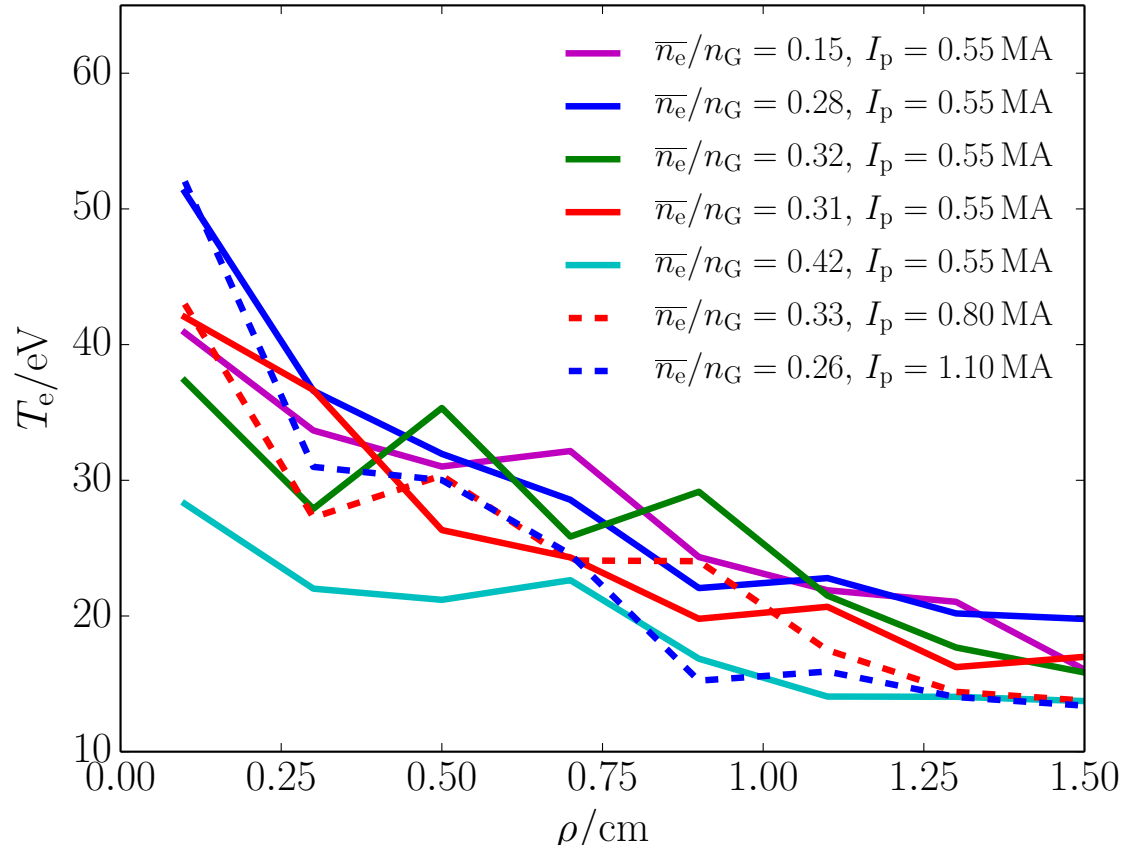


FIG. 4. Radial profiles of the electron temperature as measured by the vertical scanning probe.

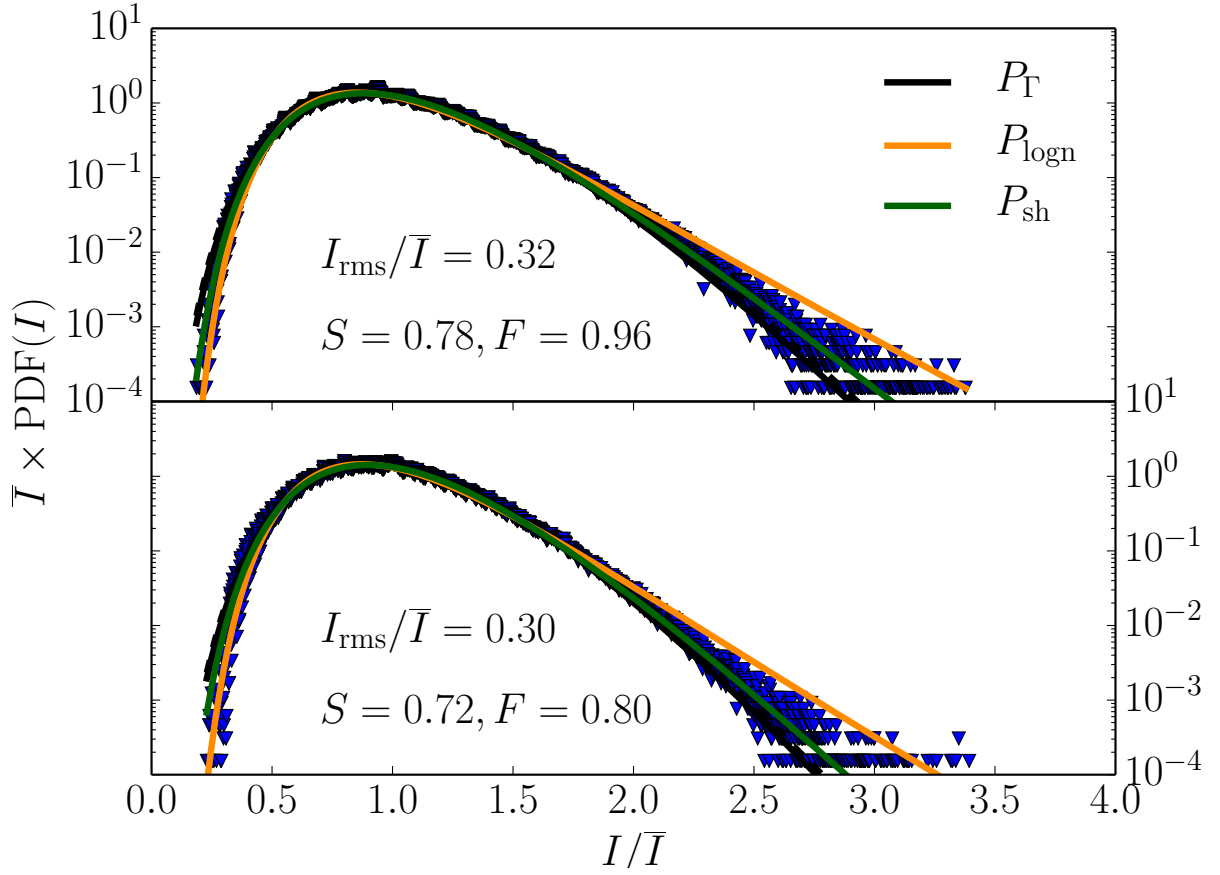


FIG. 5. Histogram of the ion saturation current as sampled by the north east pin (upper panel) and the south east pin (lower panel) of the horizontal scanning probe for $\bar{n}_e/n_G = 0.28$. Compared are best fits of estimate of Eqn. (1) (black), Eqs. (3) (orange) and 4 (dark green), as well as Eqn. (1) with scale and shape parameter estimated by Eqn. (2) of the time series (black dashed line).

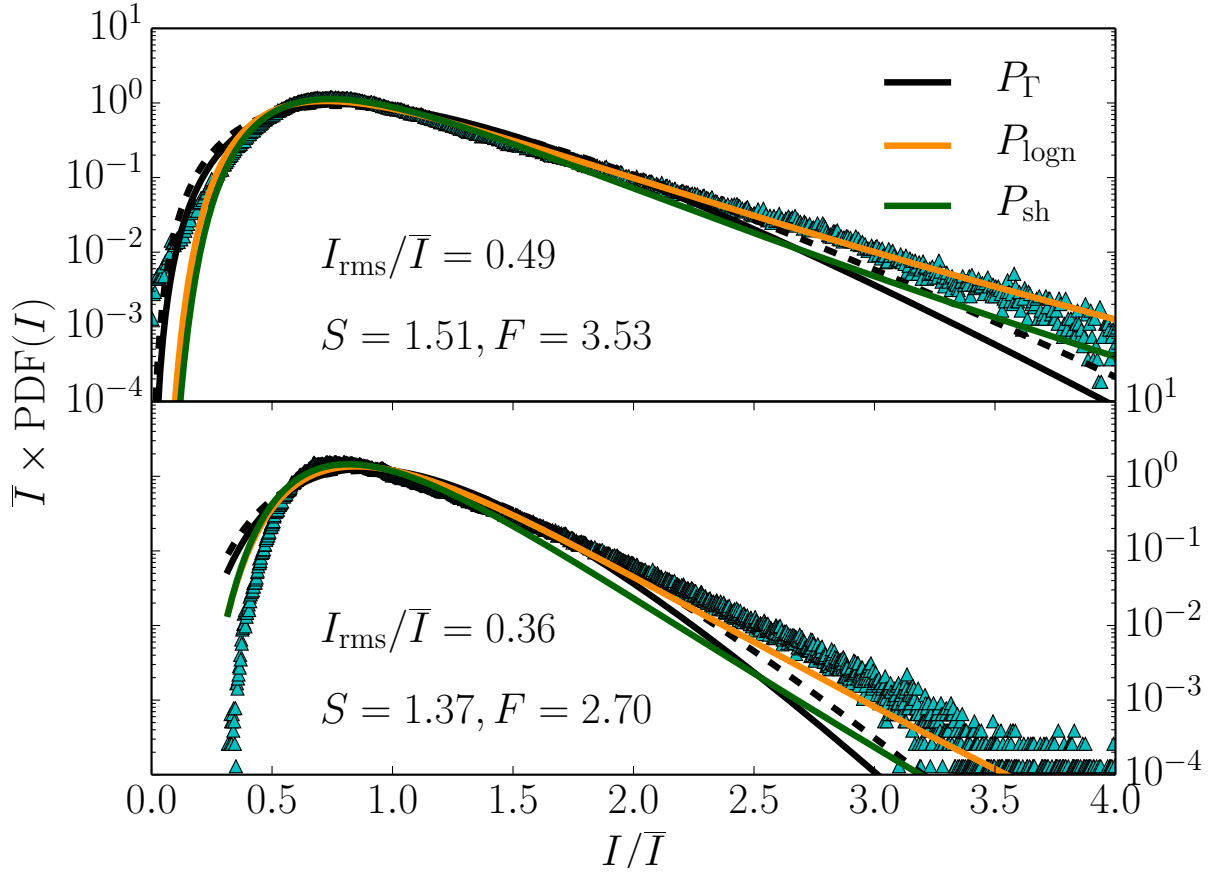


FIG. 6. Histogram of the ion saturation current as sampled by the north east pin (upper panel) and the south east pin (lower panel) of the horizontal scanning probe for $\bar{n}_e/n_G = 0.42$. Compared are best fits of estimate of Eqn. (1) (black), Eqs. (3) (orange) and 4 (dark green), as well as Eqn. (1) with scale and shape parameter estimated by Eqn. (2) of the time series (black dashed line).

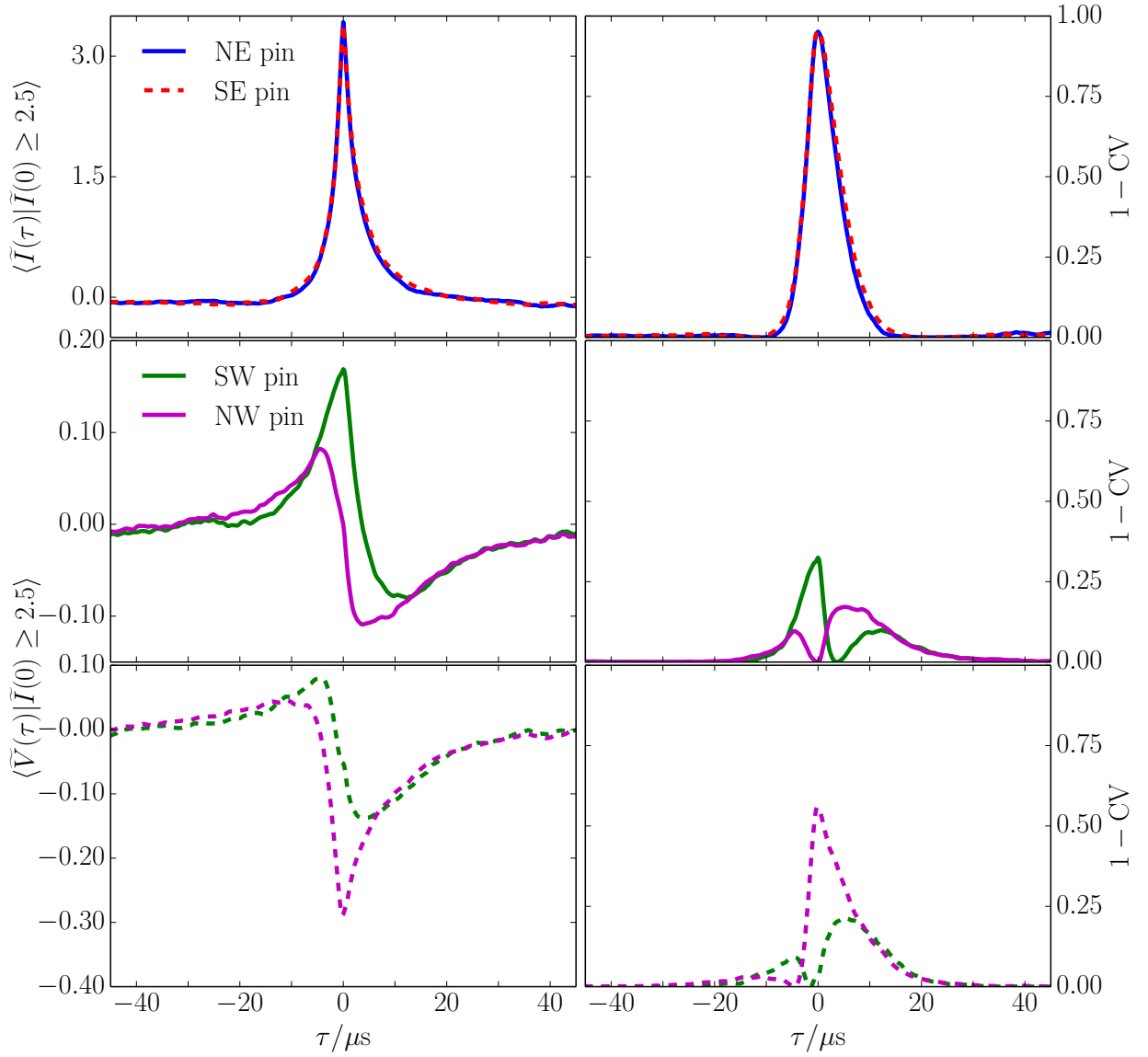


FIG. 7. Conditionally averaged burst shape and conditional variance (upper row), floating potential when triggered by bursts on the north-east pin(middle row), and floating potential when triggered by bursts on the south-east pin(bottom row), $\bar{n}_e/n_G = 0.28$.

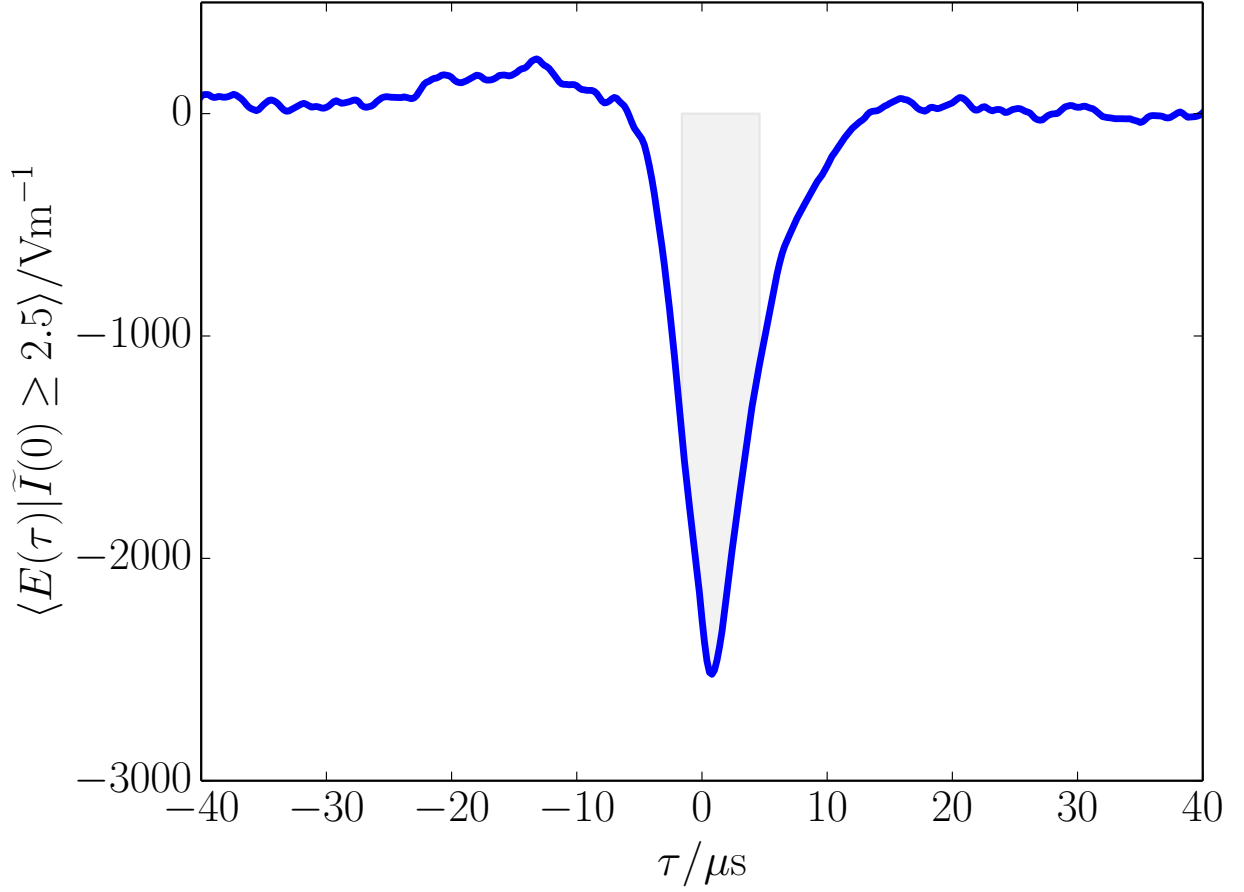


FIG. 8. Conditionally averaged electric field between the north-west and south-west electrode when triggered by bursts on the north-east pin for the discharge with $\bar{n}_e/n_G = 0.28$. The gray area corresponds to the interval $[-\tau_r : \tau_d]$, around the peak and is used to find the average electric field during a blob traversal.

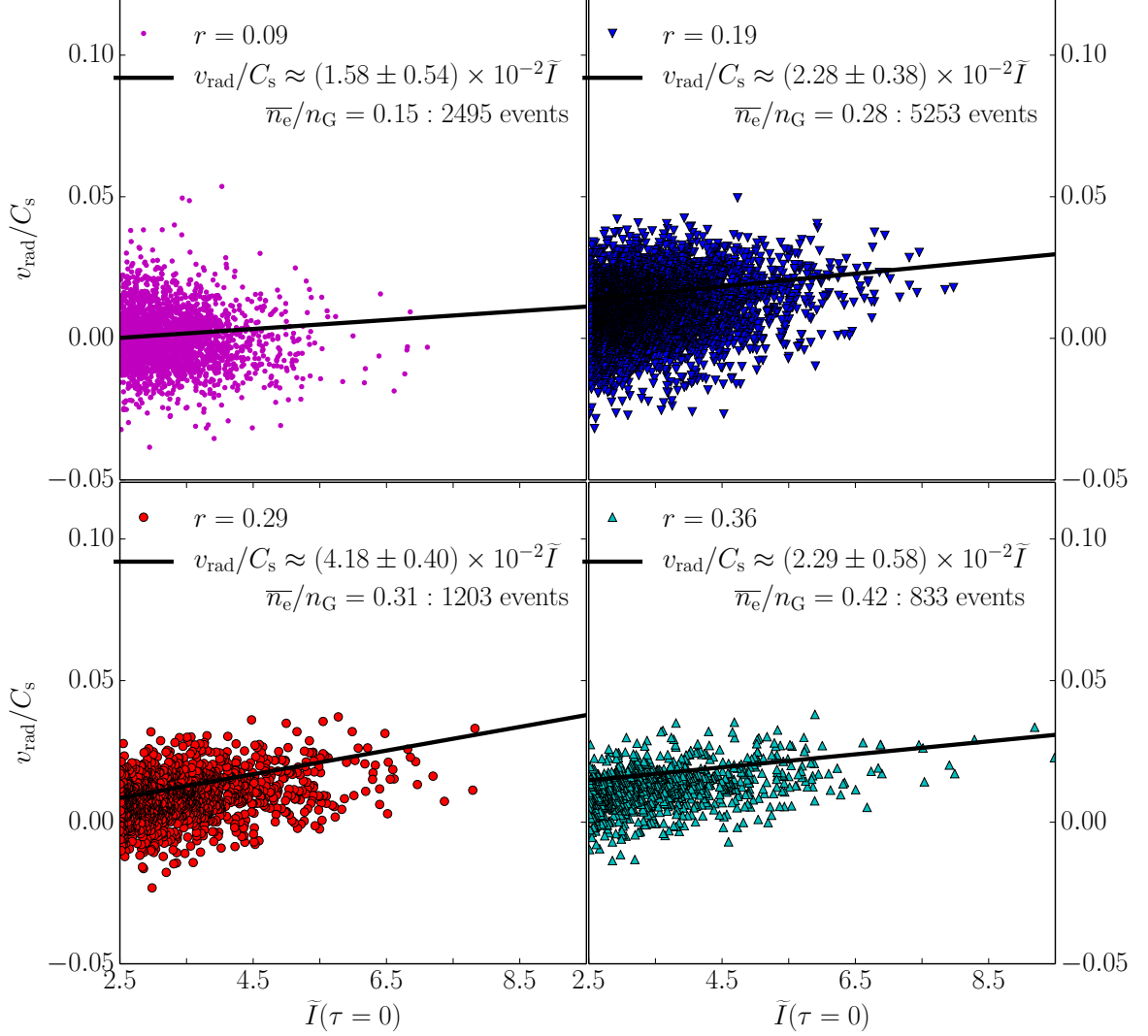


FIG. 9. Estimated radial velocity as a function of normalized burst amplitude. The legend shows the value of the Pearson sample correlation coefficient and the slope denotes the best fit of a linear model. Upper left panel: Horizontal scanning probe dwelled in the near scrape-off layer, All other panels: Horizontal scanning probe dwelled in the far scrape-off layer

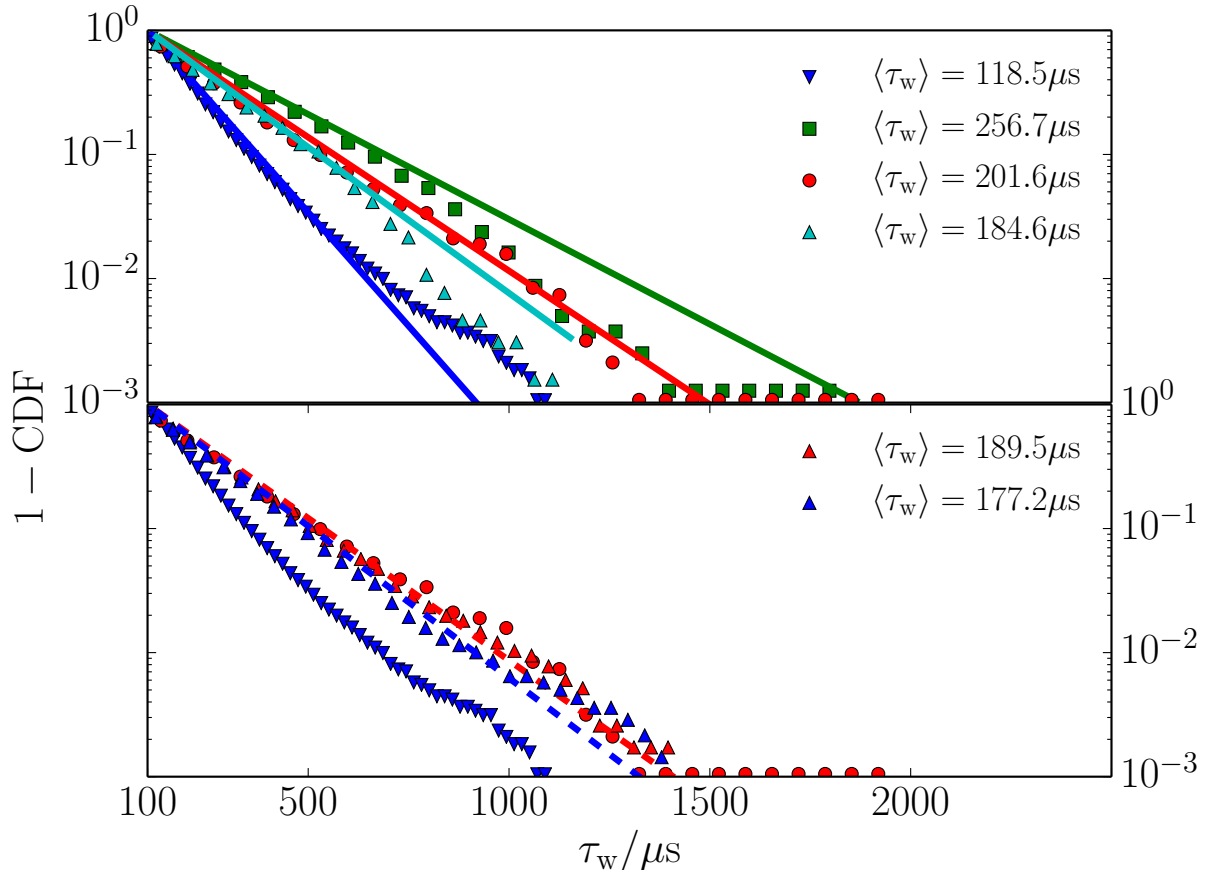


FIG. 10. Distribution of waiting times between successive large amplitude burst events in the ion saturation current time series as measured by the horizontal scanning probe.

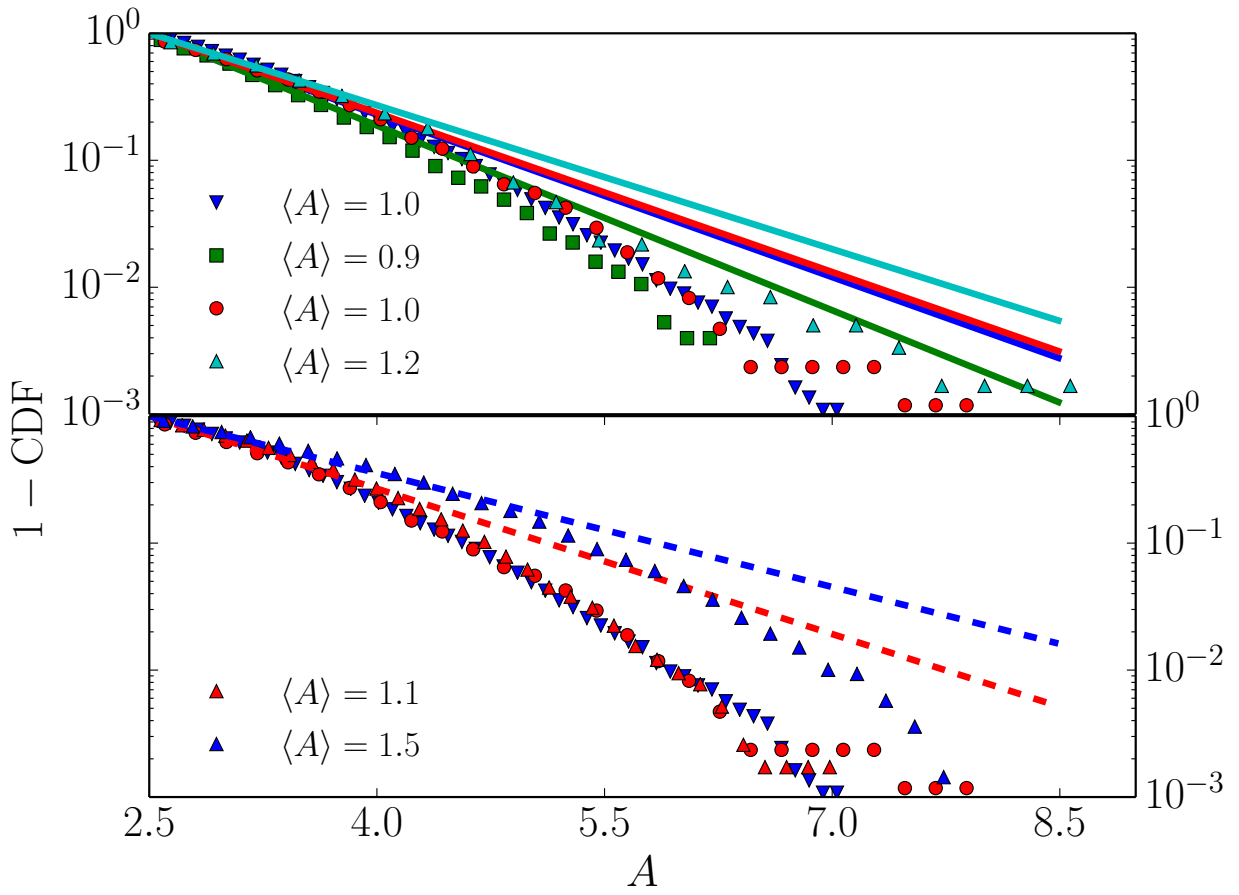


FIG. 11. Amplitude distribution of burst events in the ion saturation current time series as measured by the horizontal scanning probe.

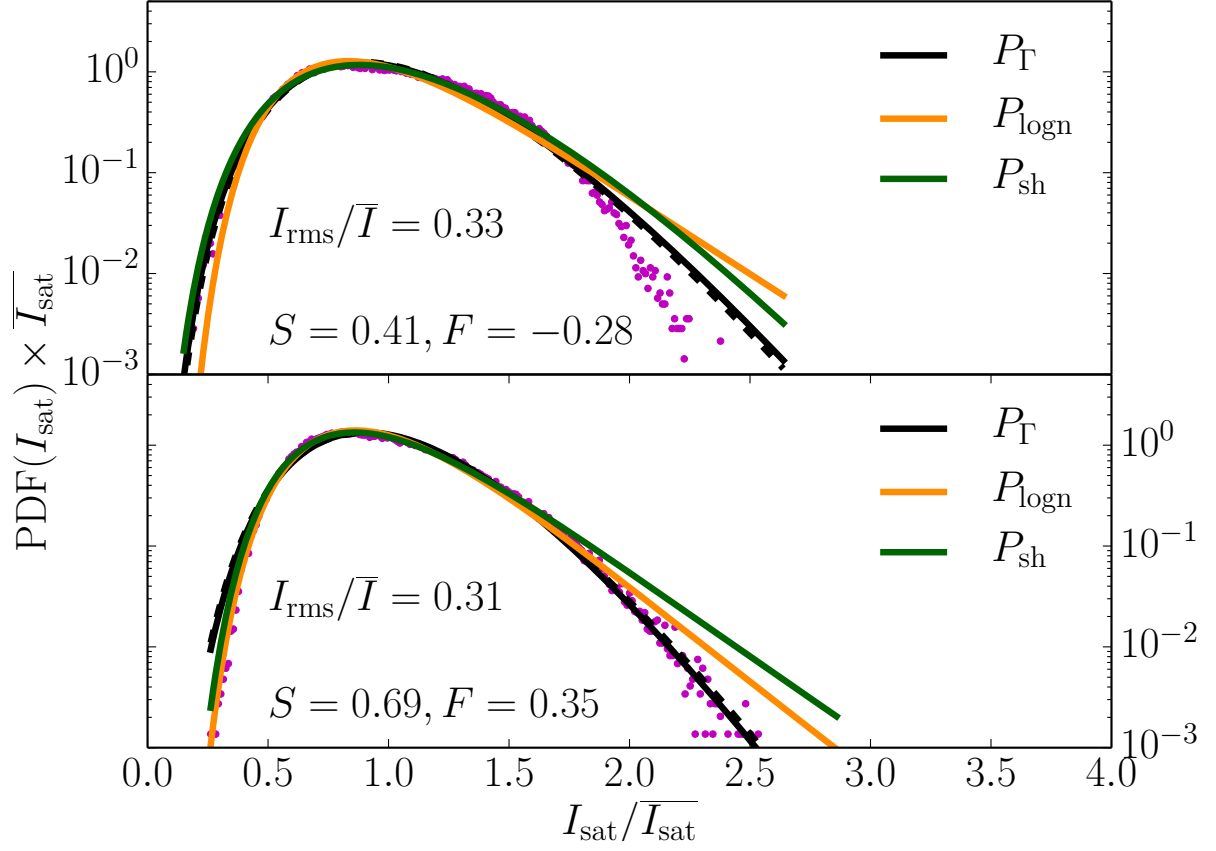


FIG. 12. Histogram of the ion saturation current as sampled by divertor probes 9 (upper panel), and 10 (lower panel) for the discharge with $\bar{n}_e/n_G = 0.15$. Compared are best fits of Eqn. (1) (black), Eqs. (3) (orange) and 4 (dark green), as well as Eqn. (1) with scale and shape parameter estimated by the statistics of the time series (black dashed line).

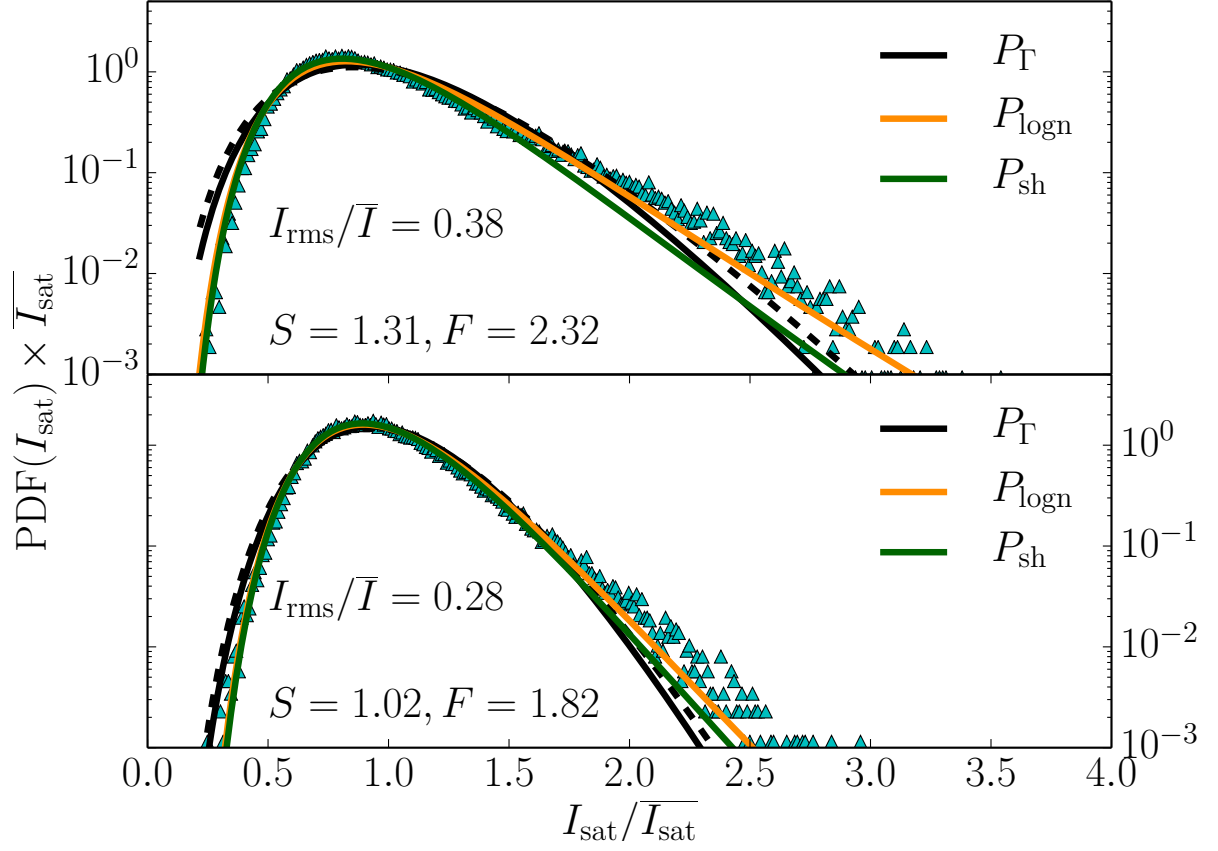


FIG. 13. Histogram of the ion saturation current as sampled by divertor probes 9 (upper panel), and 10 (lower panel) for the discharge with $\bar{n}_e/n_G = 0.42$. Compared are best fits of Eqn. (1) (black), Eqs. (3) (orange) and 4 (dark green), as well as Eqn. (1) with scale and shape parameter estimated by the statistics of the time series (black dashed line).

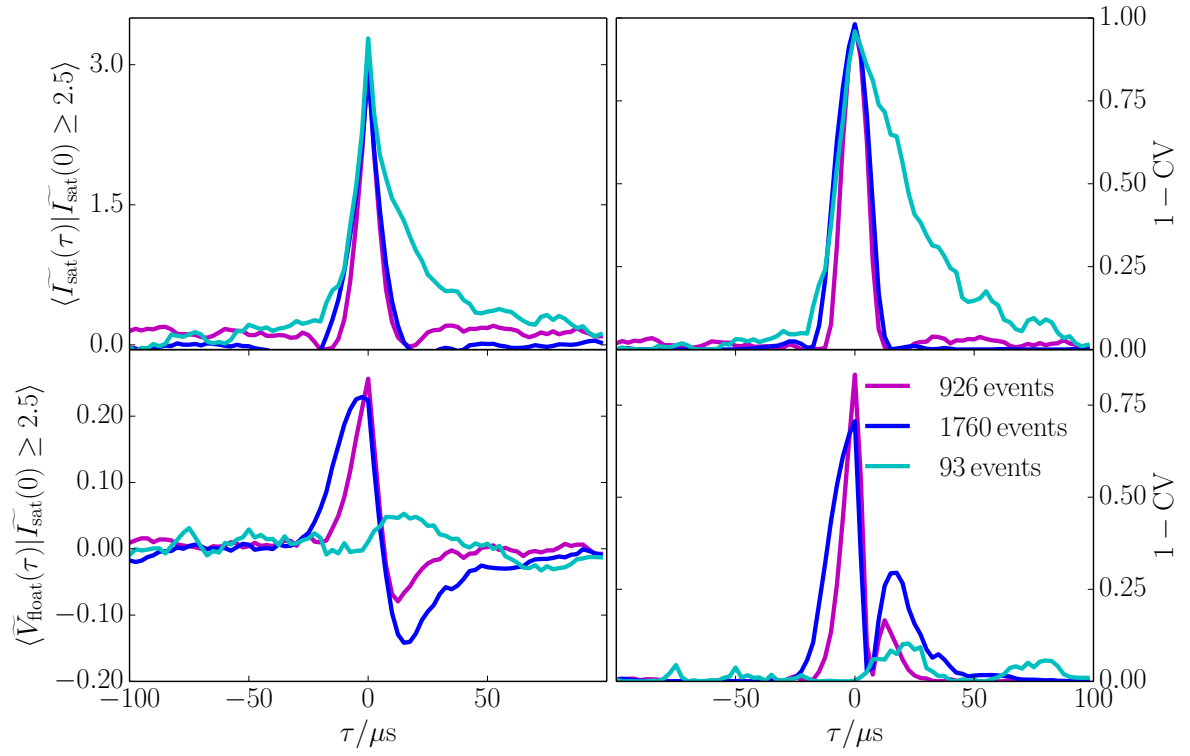


FIG. 14. Conditionally averaged burst shape and conditional variance (upper row), and floating potential structure with conditional variance (bottom row), as measured by divertor probe 10.

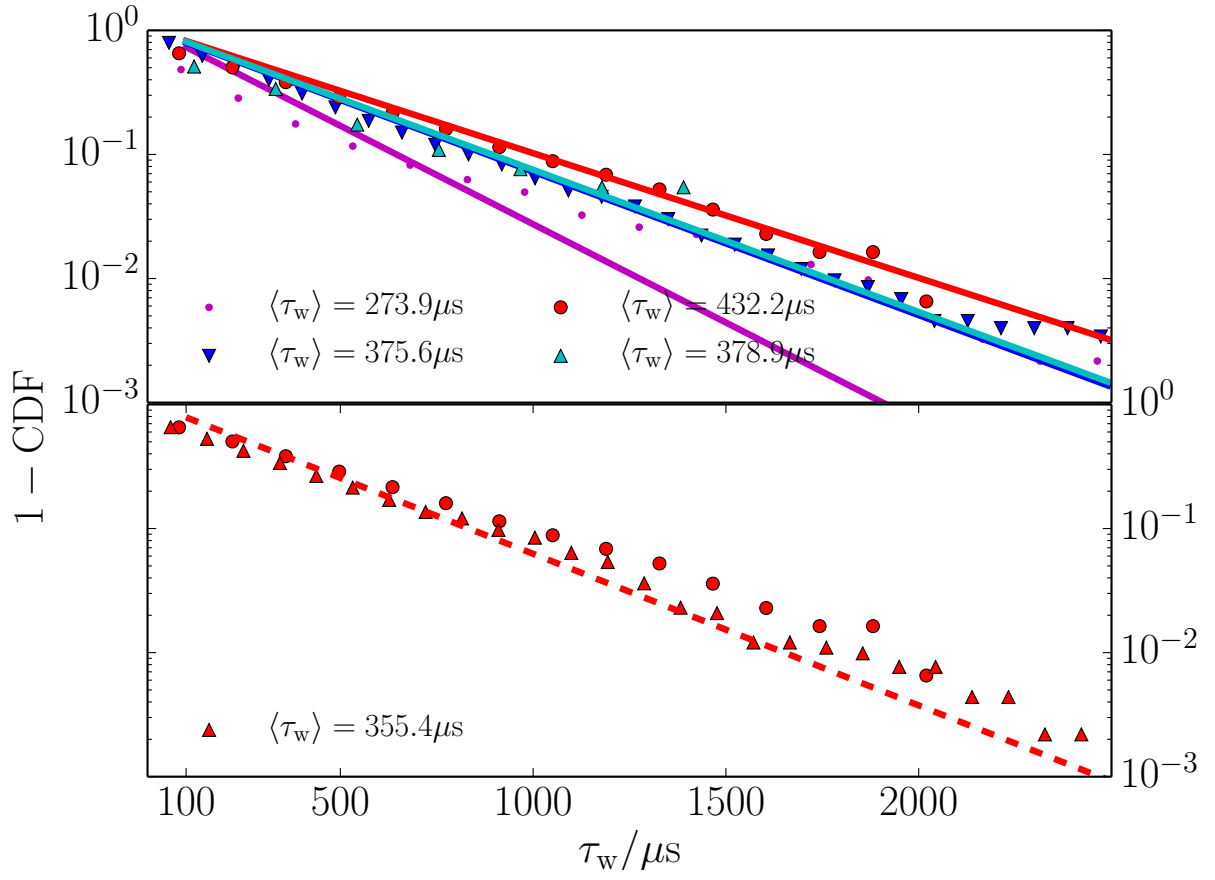


FIG. 15. Waiting time distribution of burst events with amplitude exceeding 2.5 times the RMS value as measured at divertor probe 10.

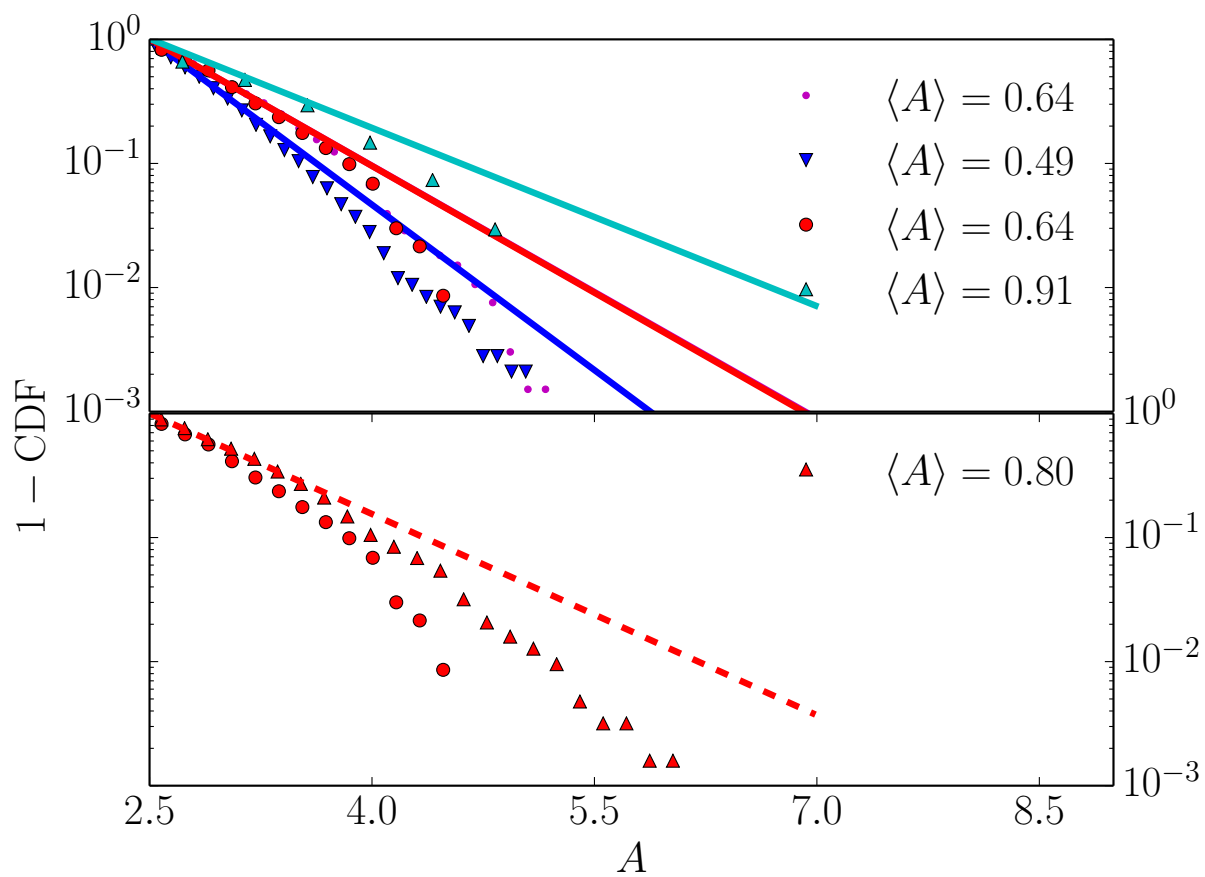


FIG. 16. Burst amplitude distribution for amplitude events exceeding 2.5 times the RMS value as measured at divertor probe 10.

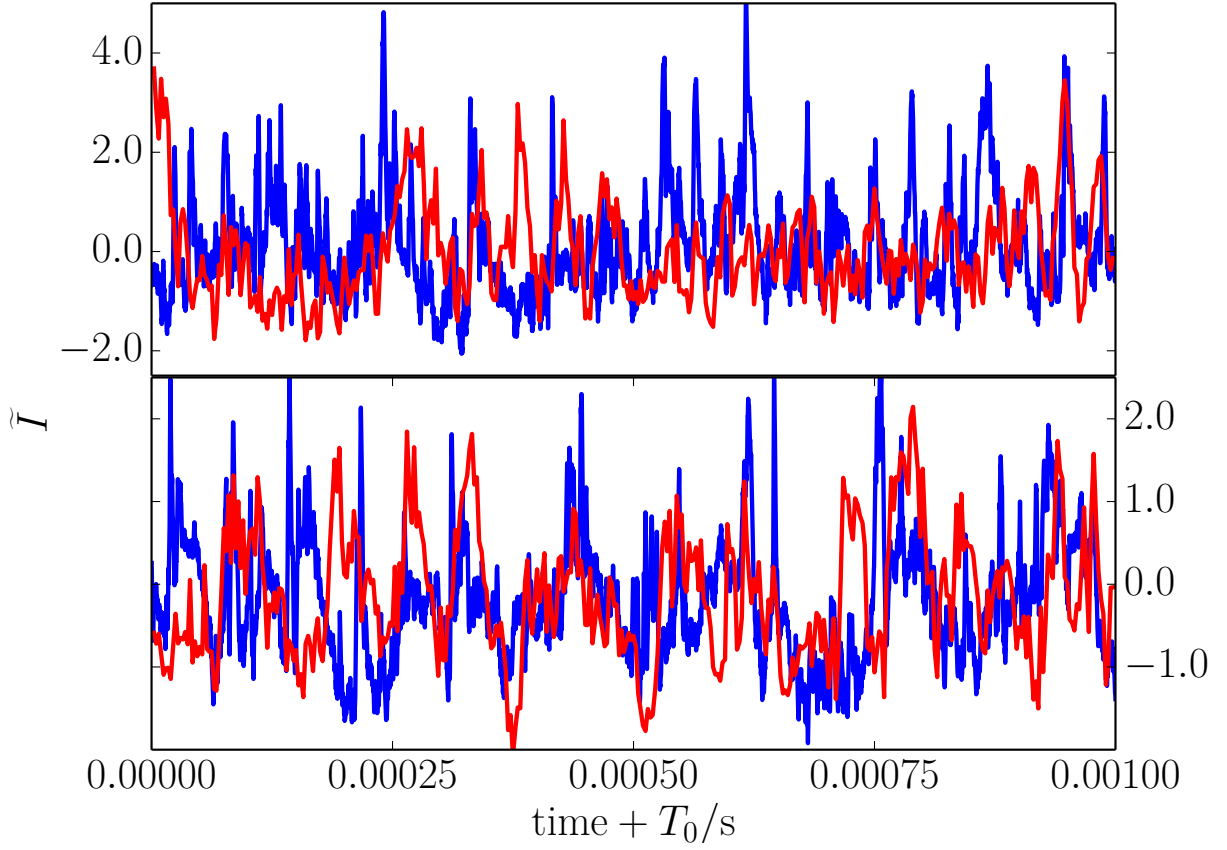


FIG. 17. Time series of the normalized ion saturation current as measured by the horizontal scanning probe (blue) and the outermost divertor probe (red) for discharges with $\bar{n}_e/n_G = 0.28$ (upper panel) and $\bar{n}_e/n_G = 0.42$ (lower panel). The time offset is $T_0 = 0.9$ s and $T_0 = 0.55$ s for the upper and lower panel respectively.

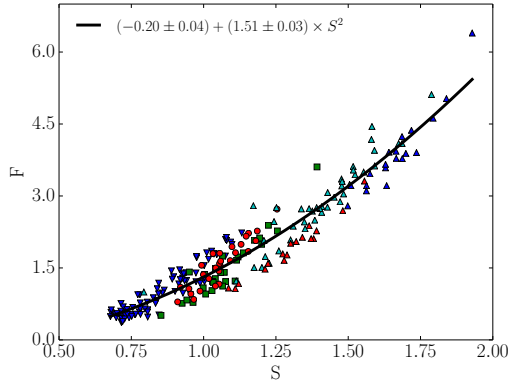


FIG. 18. Coefficients of skewness and excess kurtosis computed for 20ms long sub samples of the ion saturation current as sampled by the both pins of the horizontal scanning probe.

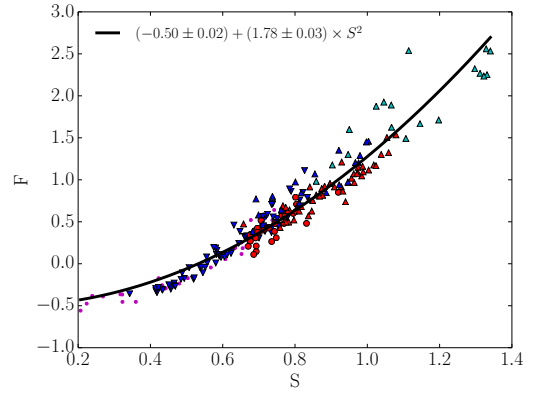


FIG. 19. Coefficients of skewness and excess kurtosis computed for 20ms long sub samples of the ion saturation current as sampled by the outer most divertor probe.

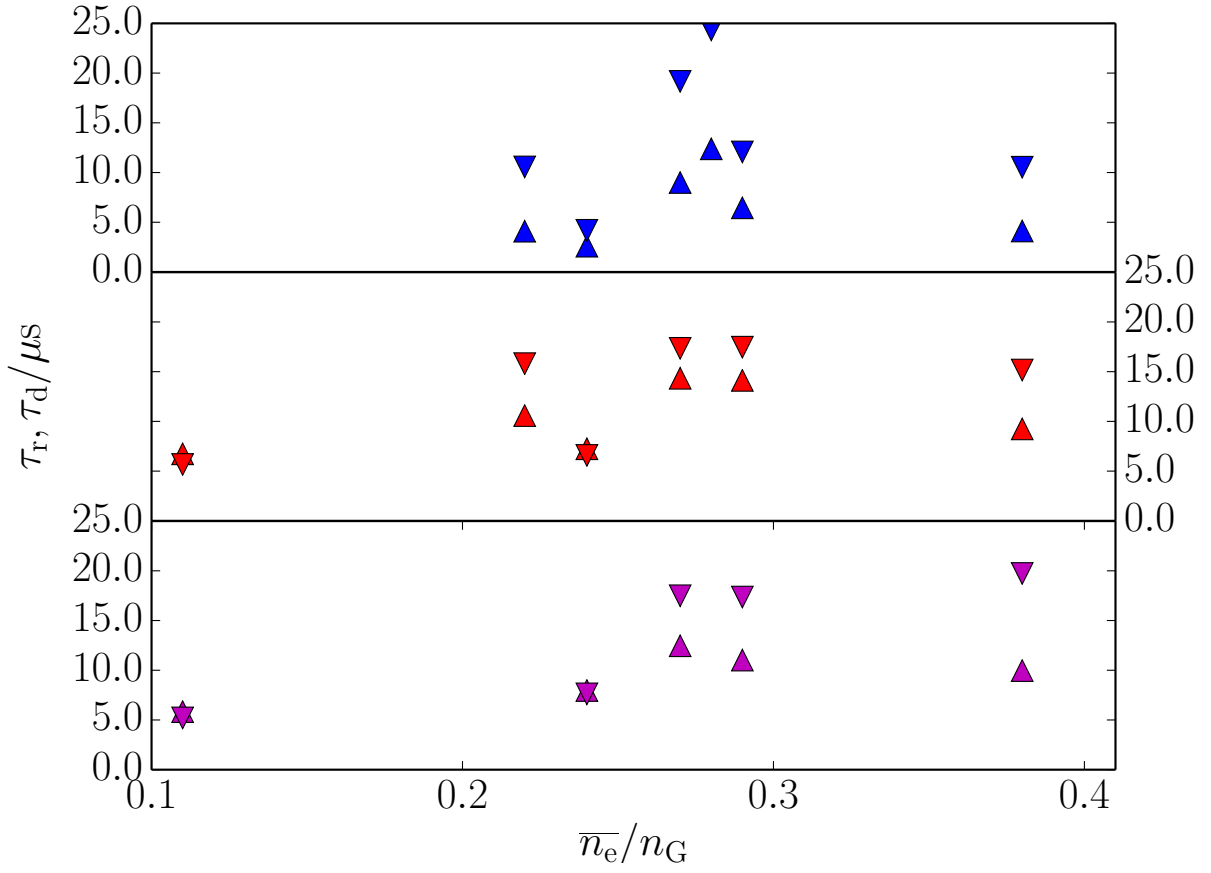


FIG. 20. Scale length of exponential fits on the conditionally averaged burst shape, as measured by the horizontal scanning probe (upper panel), divertor probe 9 (middle panel) and divertor probe 10 (lower panel). Triangles pointing up denote rise times τ_r and triangles pointing down denote decay times. τ_d .

-
- * E-mail:ralph.kube@uit.no
- ¹ F. Sattin, N. Vianello, and M. Valisa, *Physics of Plasmas* (1994-present) **11**, 5032 (2004).
- ² A. J. Wootton, B. A. Carreras, H. Matsumoto, K. McGuire, W. A. Peebles, C. P. Ritz, P. W. Terry, and S. J. Zweben, *Physics of Fluids B: Plasma Physics* **2**, 2879 (1990).
- ³ S. I. Krasheninnikov, *Physics Letters A* **283**, 368 (2001).
- ⁴ J. A. Boedo, D. Rudakov, R. Moyer, S. Krasheninnikov, D. Whyte, G. McKee, G. Tynan, M. Schaffer, P. Stangeby, P. West, S. Allen, T. Evans, R. Fonck, E. Hollmann, A. Leonard, A. Mahdavi, G. Porter, M. Tillack, and G. Antar, *Physics of Plasmas* **8**, 4826 (2001).
- ⁵ J. A. Boedo, D. L. Rudakov, R. A. Moyer, G. R. McKee, R. J. Colchin, M. J. Schaffer, P. G. Stangeby, W. P. West, S. L. Allen, T. E. Evans, R. J. Fonck, E. M. Hollmann, S. Krasheninnikov, A. W. Leonard, W. Nevins, M. A. Mahdavi, G. D. Porter, G. R. Tynan, D. G. Whyte, and X. Xu, *Physics of Plasmas* **10**, 1670 (2003).
- ⁶ D. Rudakov, J. Boedo, R. Moyer, P. Stangeby, J. Watkins, D. Whyte, L. Zeng, N. Brooks, R. Doerner, T. Evans, M. Fenstermacher, M. Groth, E. Hollmann, S. Krasheninnikov, C. Lasnier, A. Leonard, M. Mahdavi, G. McKee, A. McLean, A. Pigarov, W. Wampler, G. Wang, W. West, and C. Wong, *Nuclear Fusion* **45**, 1589 (2005).
- ⁷ O. E. Garcia, N. H. Bian, V. Naulin, A. H. Nielsen, and J. J. Rasmussen, *Physica Scripta* **2006**, 104 (2006).
- ⁸ W. Fundamenski, O. Garcia, V. Naulin, R. Pitts, A. Nielsen, J. J. Rasmussen, J. Horacek, J. Graves, and J. E. contributors, *Nuclear Fusion* **47**, 417 (2007).
- ⁹ O. E. Garcia, N. H. Bian, and W. Fundamenski, *Physics of Plasmas* **13**, 082309 (2006).
- ¹⁰ J. R. Myra, D. A. Russell, and D. A. D'Ippolito, *Physics of Plasmas* **13**, 112502 (2006).
- ¹¹ D. A. Russell, D. A. D'Ippolito, J. R. Myra, W. M. Nevins, and X. Q. Xu, *Phys. Rev. Lett.* **93**, 265001 (2004).
- ¹² S. Krasheninnikov, D. Rutovi, and Y. Guanghai, *Journal of Plasma Fusion Research Series* **6**, 139 (2004).
- ¹³ D. D. Ryutov and R. H. Cohen, *Contributions to Plasma Physics* **44**, 168 (2004).
- ¹⁴ R. Cohen, B. LaBombard, D. Ryutov, J. L. Terry, M. Umansky, X. Xu, and S. Zweben, *Nuclear Fusion* **47**, 612 (2007).

- ¹⁵ C. Theiler, I. Furno, P. Ricci, A. Fasoli, B. Labit, S. H. Müller, and G. Plyushchev, *Phys. Rev. Lett.* **103**, 065001 (2009).
- ¹⁶ R. Kube and O. E. Garcia, *Physics of Plasmas* (1994-present) **18**, 102314 (2011).
- ¹⁷ R. Kube and O. E. Garcia, *Physics of Plasmas* (1994-present) **19**, (2012).
- ¹⁸ O. Grulke, J. L. Terry, I. Cziegler, B. LaBombard, and O. E. Garcia, *Nuclear Fusion* **54**, 043012 (2014).
- ¹⁹ G. Y. Antar, P. Devynck, X. Garbet, and S. C. Luckhardt, *Physics of Plasmas* (1994-present) **8**, 1612 (2001).
- ²⁰ G. Y. Antar, G. Counsell, Y. Yu, B. Labombard, and P. Devynck, *Physics of Plasmas* **10**, 419 (2003).
- ²¹ B. P. van Milligen, R. Sánchez, B. A. Carreras, V. E. Lynch, B. LaBombard, M. A. Pedrosa, C. Hidalgo, B. Gonçalves, R. Balbín, and T. W.-A. Team, *Physics of Plasmas* (1994-present) **12**, 052507 (2005).
- ²² D. L. Rudakov, J. A. Boedo, R. A. Moyer, S. Krasheninnikov, A. W. Leonard, M. A. Mahdavi, G. R. McKee, G. D. Porter, P. C. Stangeby, J. G. Watkins, W. P. West, D. G. Whyte, and G. Antar, *Plasma Physics and Controlled Fusion* **44**, 717 (2002).
- ²³ G. S. Kirnev, V. P. Budaev, S. A. Grashin, E. V. Gerasimov, and L. N. Khimchenko, *Plasma Physics and Controlled Fusion* **46**, 621 (2004).
- ²⁴ Y. H. Xu, S. Jachmich, R. R. Weynants, and the TEXTOR team, *Plasma Physics and Controlled Fusion* **47**, 1841 (2005).
- ²⁵ O. E. Garcia, J. Horacek, R. A. Pitts, A. H. Nielsen, W. Fundamenski, J. P. Graves, V. Naulin, and J. J. Rasmussen, *Plasma Physics and Controlled Fusion* **48**, L1 (2006).
- ²⁶ O. Garcia, J. Horacek, R. Pitts, A. Nielsen, W. Fundamenski, V. Naulin, and J. J. Rasmussen, *Nuclear Fusion* **47**, 667 (2007).
- ²⁷ O. Grulke, J. L. Terry, B. LaBombard, and S. J. Zweben, *Physics of Plasmas* **13**, 012306 (2006).
- ²⁸ P. Devynck, J. Brotankova, P. Peleman, M. Spolaore, H. Figueiredo, M. Hron, G. Kirnev, E. Martines, J. Stockel, G. Van Oost, and V. Weinzettl, *Physics of Plasmas* (1994-present) **13**, 102505 (2006).
- ²⁹ T. A. Carter, *Physics of Plasmas* (1994-present) **13**, 010701 (2006).
- ³⁰ G. Y. Antar, S. I. Krasheninnikov, P. Devynck, R. P. Doerner, E. M. Hollmann, J. A. Boedo, S. C. Luckhardt, and R. W. Conn, *Phys. Rev. Lett.* **87**, 065001 (2001).

- ³¹ J. P. Graves, J. Horacek, R. A. Pitts, and K. I. Hopcraft, *Plasma Physics and Controlled Fusion* **47**, L1 (2005).
- ³² B. Labit, I. Furno, A. Fasoli, A. Diallo, S. H. Müller, G. Plyushchev, M. Podestà, and F. M. Poli, *Phys. Rev. Lett.* **98**, 255002 (2007).
- ³³ J. Rice, *Advances in Applied Probability* **9**, pp. 553 (1977).
- ³⁴ O. E. Garcia, *Phys. Rev. Lett.* **108**, 265001 (2012).
- ³⁵ O. E. Garcia, S. M. Fritzner, R. Kube, I. Cziegler, B. LaBombard, and J. L. Terry, *Phys. Plasmas* **20**, 055901 (2013).
- ³⁶ H. L. Pécseli and J. Trulsen, *Physics of Fluids B: Plasma Physics (1989-1993)* **1**, 1616 (1989).
- ³⁷ F. J. Øynes, H. L. Pecseli, and K. Rypdal, *Phys. Rev. Lett.* **75**, 81 (1995).
- ³⁸ L. Lao, H. S. John, R. Stambaugh, A. Kellman, and W. Pfeiffer, *Nuclear Fusion* **25**, 1611 (1985).
- ³⁹ R. S. Granetz, I. H. Hutchinson, J. Gerolamo, W. Pina, and C. Tsui, *Review of Scientific Instruments* **61**, 2967 (1990).
- ⁴⁰ N. Smick and B. LaBombard, *Review of Scientific Instruments* **80**, 023502 (2009).
- ⁴¹ N. Smick, B. LaBombard, and I. Hutchinson, *Nuclear Fusion* **53**, 023001 (2013).
- ⁴² B. LaBombard, R. L. Boivin, M. Greenwald, J. Hughes, B. Lipschultz, D. Mossessian, C. S. Pitcher, J. L. Terry, S. J. Zweben, and the Alcator C-Mod Group (Alcator Group), *Physics of Plasmas* **8**, 2107 (2001).
- ⁴³ R. Fraile and E. García-Ortega, *Journal of Applied Meteorology*, *Journal of Applied Meteorology* **44**, 1620 (2005).
- ⁴⁴ B. LaBombard, J. Goetz, C. Kurz, D. Jablonski, B. Lipschultz, G. McCracken, A. Niemczewski, R. L. Boivin, F. Bombarda, C. Christensen, S. Fairfax, C. Fiore, D. Garnier, M. Graf, S. Golovato, R. Granetz, M. Greenwald, S. Horne, A. Hubbard, I. Hutchinson, J. Irby, J. Kesner, T. Luke, E. Marmor, M. May, P. O'Shea, M. Porkolab, J. Reardon, J. Rice, J. Schachter, J. Snipes, P. Stek, Y. Takase, J. Terry, G. Tinios, R. Watterson, B. Welch, and S. Wolfe, *Physics of Plasmas (1994-present)* **2**, 2242 (1995).
- ⁴⁵ J. R. Myra, D. A. D'Ippolito, S. I. Krasheninnikov, and G. Q. Yu, *Physics of Plasmas* **11**, 4267 (2004).
- ⁴⁶ M. Agostini, J. Terry, P. Scarin, and S. Zweben, *Nuclear Fusion* **51**, 053020 (2011).
- ⁴⁷ R. Kube, O. Garcia, B. LaBombard, J. Terry, and S. Zweben, *Journal of Nuclear Materials*

438, Supplement, S505 (2013), proceedings of the 20th International Conference on Plasma-Surface Interactions in Controlled Fusion Devices.